

# Direct numerical simulation of Particle Clustering and Turbulence Modulation: An Eulerian Approach

Ajay Dhankarghare<sup>1</sup>, and Yuval Dagan<sup>1†</sup>

<sup>1</sup>Faculty of Aerospace Engineering, Technion - Israel Institute of Technology, Haifa, 3200003, Israel

We present a new Eulerian framework for the computation of turbulent compressible multiphase channel flows, specifically to assess turbulence modulation by dispersed particulate matter. By combining a modified low-dissipation numerical scheme for the carrier flow and a quadrature moment-based method for the particle phase, the turbulent statistics of the carrier flow and the fluctuations of the particle phase may be obtained as both are resolved as coupled fields. Using direct numerical simulations, we demonstrate how this method resolves the turbulent statistics, kinetic energy, and drag modulation for moderate Reynolds numbers channel flows for the first time. Validation of our approach to the turbulent clean flow proves the applicability of the carrier flow low dissipation scheme for relatively low Mach number compressible flows. This study also rationalizes the computed drag modulation results using a simplified analytical approach, revealing how the particle migration towards the wall can affect the drag between the two phases at different Stokes numbers and particle loadings. Using our Eulerian approach, we also show the complex interplay between the particles and flow turbulence fluctuations by capturing the preferential clustering of particles in the turbulence streaks. This interplay leads to turbulent flow modulations similar to recent observations reported in prior computational works using Lagrangian simulations. Our study extends the applicability of Eulerian approaches to accurately study particle-fluid interactions in compressible turbulent flows by explicitly calculating the energy equations for both the particle phase and the carrier fluid motion. Since the formulation is compressible and includes energy equations for both the particle and carrier flow fields, future studies for lower and higher Mach number flows and heat and mass transfer may be simulated using this methodology.

## 1. Introduction

Dispersed particle-laden turbulent flows find application in many environmental, atmospheric, and engineering fields. Adding particles to the flow leads to various phenomena such as inter-particle collisions, particle-flow interactions, wall-particle collisions, particle clustering and migration. All these phenomena play an important role in modulating the turbulence and drag.

Particles in inhomogeneous turbulent flows tend to migrate towards the wall by a phenomenon known as turbophoresis. This observation was first reported by Caporaloni *et al.* (1975) and later studied by Reeks (1983). McLaughlin (1989) observed a similar behavior of the particles in the vertical channel turbulent flow. He observed the near wall accumulation of particles even in the absence of Saffmann lift force Saffman (1965). Marchioli & Soldati (2002) examined the effect of flow turbulence on particle

† Email address for correspondence: yuvalda@technion.ac.il

transfer to the wall. They found that strong coherent sweep and ejection events are the main mechanisms transferring the particles toward the wall. Sikovsky (2014) and Johnson *et al.* (2020) pointed out the power-law shape of particle concentrations in the viscous sublayer.

Not only do the particles migrate towards the wall, but they also show a tendency to preferentially cluster in turbulence streaks. Sardina *et al.* (2012) showed that turbophoresis and preferential clustering of particles occur simultaneously in wall-bounded flows. Squires & Eaton (1991) and Eaton & Fessler (1994) observed that in isotropic turbulence, smaller particles show a higher tendency to preferential cluster in the low-speed streaks, while Marchioli & Soldati (2002) and Fong *et al.* (2019) observed the accumulation of larger particles in high-speed streaks near the channel wall. Peng *et al.* (2024), in their simulation of sedimenting flow, showed that larger particles could accumulate in either low-speed streaks or high-speed streaks. Recently, Dave & Kasbaoui (2023) showed the accumulation of smaller particles in the low-speed streaks near the channel wall. However, the effects of particle Stokes number and mass loading were not clear from their Direct Numerical Simulations (DNS). Thus, it can be understood that the streak preference of particles for clustering depends on the particle Stokes number. However, it is still required to further this knowledge on the combined effect of particle mass loading and particle Stokes number on particle preferential clustering in a turbulent channel flow.

Particles' migration toward the wall and their preferential clustering in the turbulence streaks can directly or indirectly affect the flow dynamics by various phenomena. The addition of particles has been known to modulate the flow turbulence. Zhao *et al.* (2013), Zhou *et al.* (2020), and Dave & Kasbaoui (2023) signified the role of preferential clustering of particles near the wall in modulating the flow turbulence. Kulick *et al.* (1994) showed that in a particle-laden vertical channel flow, turbulence attenuation increases with an increase in Stokes number and particle mass loading. The attenuation was more at the channel center than near the wall. The authors also pointed out that the transverse fluctuations, being at a higher frequency than the streamwise fluctuations, were attenuated more by particles that were less responsive to high-frequency fluctuations. Squires & Eaton (1994) found that increased particle clustering causes an extra dissipation of the transverse fluctuations. Vreman *et al.* (2009) and Zhao *et al.* (2010) observed that streamwise turbulence fluctuations were enhanced while the wall-normal and spanwise fluctuations were damped by the particles. Though in the study by Zhou *et al.* (2020), transverse fluctuations were damped, streamwise turbulence showed non-monotonic behavior along the normal distance from the wall. While there was a suppression of streamwise fluctuations near the wall, the particles enhanced it for  $y^+ = 40$ . In contrast, Kussin & Sommerfeld (2002) found that the streamwise turbulence was suppressed more than the wall-normal ones. However, their study included various effects like gravity in the horizontal channel, which can cause a loss in particle concentration symmetry across the channel width and affect particle motion. Moreover, the deviation in the particle diameter from the mean diameter was at least  $\pm 30\mu\text{m}$ . All these factors may complicate the analysis, and thus, a conclusive interpretation of the influence dispersed particles have on modulating turbulent fluctuations remains elusive.

From these observations, it is plausible that the non-uniform presence of particles along the channel height can affect turbulence differently at different locations. Zhao *et al.* (2013) showed the non-uniform particle drag on the fluid along the channel height, which can significantly modulate turbulence. The authors argued that the non-uniformity in drag is due to turbophoresis. Lee & Lee (2015) observed similar inhomogeneity in the particle drag profile. They demonstrated the effect of particle Stokes number on the drag

near the wall. However, the study did not address the drag profile away from the wall. Dave & Kasbaoui (2023) demonstrated that different particle mass loadings can cause the wall accumulation of particles even when the Stokes number is the same. Thus, it can be expected that the drag profile of a particle-laden flow having the same Stokes number can be modified by changing the particle loading. This will be explored in the present study.

The analysis of dispersed particles in multiphase flow using high-fidelity simulations may require the implementation of Lagrangian particle tracking (Balachandar & Eaton 2010*a*). Using simplified theoretical flow models, one may employ Lagrangian methods to track the particle and droplet trajectories and study their dispersion (Marcu & Meiburg 1996*b,a*; Marcu *et al.* 1996) and entrapment within coherent flow structures (Marcu *et al.* 1995; IJzermans & Hagmeijer 2006; Angilella 2010; Dagan 2021; Avni & Dagan 2022*b*; Ravichandran & Govindarajan 2022; Avni & Dagan 2023*a,b*). Following such a simplified approach allows the isolation of specific transport mechanisms, including oscillatory flows (Dagan *et al.* 2017*a,b*, 2018), aerosol formation (Avni & Dagan 2022*a*), and particle structures (Yerasi *et al.* 2022), while studying their influence on the particle dynamics. However, incorporating detailed models for such cases might result in computationally intensive modeling, even for relatively simple setups. The approach solves the equation for each particle. This may restrict the use of the approach while dealing with an extremely large number of particles due to its high computation cost. Furthermore, simulating the particles with low Stokes numbers adds to the cost as the low inertia particles may impose strict limitations on the maximum numerical time step. Salman & Soteriou (2004) demonstrated that the Lagrangian procedure might not converge under mesh refinement, which can be problematic when the mesh used is non-uniform, when the mesh size is less than the size of the particles, or when polydisperse particles are used. Many intriguing phenomena that result from particle-fluid interactions in a turbulent channel flow, such as turbophoresis, preferential clustering, uneven drag, and turbulence modulation, have been studied using the Lagrangian approach. Statistical study of these phenomena requires resolving the fluctuations in particle properties that might be difficult to estimate using the Lagrangian approach.

The Eulerian approach to simulating the particle phase offers a more efficient and significantly less computationally expensive alternative. Earlier works (Zhang & Prosperetti 1994; Druzhinin 1994, 1995; Zhang & Prosperetti 1997; Mehta & Jayachandran 1998) used the Eulerian approach to simulate the dispersed-particle field. The approach assumes the average particle field inside the control volume. This allows for the simulation of the particles in the domain with a non-uniform mesh that can be smaller than the particle size. However, the averaging of the particle field limits the ability of the approach to resolve various particle phenomena like particle-trajectory crossing, particle-wall reflections, and inter-particle collisions. Furthermore, the absence of the pressure term in the particle phase transport system leads to a non-hyperbolic nature of the system that can result in numerical stiffness problems (Bouchut 1994). To overcome these limitations, Eulerian approaches were developed using higher moment methods (Desjardins *et al.* 2008; Fox *et al.* 2008; Marchisio & Fox 2013; Vié *et al.* 2015; Kasbaoui *et al.* 2019; Schneiderbauer & Saeedipour 2019; Heylmun *et al.* 2021). Studies using these methods are mostly restricted to the investigation of particle-laden flows in isotropic homogeneous turbulence, where wall reflections can be avoided. In 2020, Baker *et al.* (2020) used the Eulerian moment method approach to simulate the particle field in a vertical channel turbulent flow and compared the results with those using the Lagrangian approach. They noticed that simulations involving particles with small Stokes numbers gave similar results for the two approaches. At high Stokes number

and low mass loading, the Eulerian approach failed to predict similar results as the Lagrangian approach due to its inability to simulate a very sparsely populated particle field. The authors considered the anisotropic Gaussian distribution of the particle velocity (Kong *et al.* 2017). Fox (2012) and Baker *et al.* (2020) claimed that using this distribution with up to second-order moments of velocity can capture the anisotropic velocity of the particle phase but not the particle-trajectory crossing for which velocity moments of up to third-order were required. Though the authors showcased the effectiveness of the moment method in simulating the low Stokes particles with a significant mass loading, the ability of the method to simulate the particle field in different environments and configurations remains elusive. It is also required for the method to be able to capture the particle-trajectory crossing. This can be crucial for future studies of a very large number of particles in both compressible and incompressible flows involving various important phenomena such as heat transfer, coalescence, inter-particle collisions, combustion, evaporation, condensation, and dispersion. These phenomena can significantly affect the stability of turbulent flows (Dagan *et al.* 2015, 2016). Furthermore, it is necessary to establish the reliability of the method to capture various intriguing phenomena that result from particle-fluid interactions in a turbulent channel flow, such as uneven drag, turbophoresis, preferential clustering, and turbulence modulation.

The primary objective of this study is to introduce an Eulerian approach for the simulation of particle fields in channel flows. The goal is to show the efficacy of this approach in accurately predicting the particles' behavior in turbulent flows. Specifically, we want to resolve the particle-fluid interactions affecting turbulence modulation, drag, particle accumulation, and preferential clustering. Moreover, the capability of a compressible solver to effectively handle the flow field even in an incompressible regime ( $M < 0.3$ ) will be explored.

In the present work, the use of the quadrature-based moment method (Desjardins *et al.* 2006, 2008) has been extended to simulate dispersed particle-laden turbulent flows in a horizontal channel using the Finite Volume Method (FVM). By coupling the particle solver with the compressible solver for the fluid phase, we aim to demonstrate the effectiveness of this Eulerian method of moments in simulating dispersed particle fields in various configurations and environments in both low-speed and high-speed compressible flows. Our results show, for the first time, that this framework accurately captures the intrinsic behavior of particles and their influence on fluid dynamics, focusing on key phenomena related to fluid-particle interactions, such as particle migration toward the wall, preferential clustering of particles within turbulent streaks, fluid turbulence modulation, and the drag exerted by particles on the fluid. Furthermore, we investigate how varying the Stokes number and particle mass loading impacts these phenomena without requiring any statistical models for particle properties, as is typically needed in Lagrangian approaches. We demonstrate that the Eulerian Quadrature-Based Moment Method effectively captures the effects of Stokes number and particle mass loading on these interactions.

The paper is organized as follows. The numerical procedure is described in section 2. The section outlines the fluid transport equations and the particle moment transport equations and demonstrates the finite volume schemes used to solve these equations. Section 3 describes the flow configuration, illustrating various flow parameters of the two phases. In section 4.1, we show various turbulence statistics of the particle-free and various particle-laden channel flows. In section 4.2, the influence of particles on the fluid and particle Reynolds stress is discussed. This section also compares the particle drag acting upon the carrier fluid at various combinations of Stokes number and particle mass loading. Section 4.3 identifies the particle migration towards the wall

and preferential clustering of particles in low-speed streaks. Section 4.4 describes the presence and behavior of turbulence and particle streaks near the channel wall at various Stokes numbers and particle mass loading. Conclusions are drawn in section 5.

## 2. Numerical procedure

A GPU-accelerated in-house numerical solver is developed for DNS of turbulent flows laden with dispersed particles. The fluid is modelled as an ideal compressible gas, while the particle phase is treated as solid and dilute with no inter-particle interactions. The Stokes number is assumed to be small, allowing for the formulation of different particle moments (Desjardins *et al.* 2008), and the particle Reynolds number  $Re_p$  is assumed to be in the Stokes regime, justifying the use of Stokes drag for the two-phase interaction. Gravity and particle-particle interactions are neglected, and elastic collisions between particles and the wall are assumed. Particles are assumed to be in thermal equilibrium with the fluid at all times, so no heat transfer between the two phases is solved. Finally, the flow Prandtl number is set to 0.71.

### 2.1. Fluid phase transport equations

The following compressible transport equations for the carrier fluid phase are solved:

$$\begin{aligned}
 \frac{\partial \rho}{\partial t} + \vec{\nabla} \cdot (\rho \vec{V}) &= 0 \\
 \frac{\partial(\rho u)}{\partial t} + \vec{\nabla} \cdot (\rho u \vec{V} + P \hat{x}) &= \vec{\nabla} \cdot (\tau_{xx} \hat{x} + \tau_{xy} \hat{y} + \tau_{xz} \hat{z}) - F_{Dx} \\
 \frac{\partial(\rho v)}{\partial t} + \vec{\nabla} \cdot (\rho v \vec{V} + P \hat{y}) &= \vec{\nabla} \cdot (\tau_{xy} \hat{x} + \tau_{yy} \hat{y} + \tau_{yz} \hat{z}) - F_{Dy} \\
 \frac{\partial(\rho w)}{\partial t} + \vec{\nabla} \cdot (\rho w \vec{V} + P \hat{z}) &= \vec{\nabla} \cdot (\tau_{xz} \hat{x} + \tau_{yz} \hat{y} + \tau_{zz} \hat{z}) - F_{Dz} \\
 \frac{\partial(\rho e)}{\partial t} + \vec{\nabla} \cdot ((\rho e + P) \vec{V}) &= \vec{\nabla} \cdot (q_x \hat{x} + q_y \hat{y} + q_z \hat{z}) - E_D
 \end{aligned} \tag{2.1}$$

$\vec{F}_D (= F_{Dx} \hat{x} + F_{Dy} \hat{y} + F_{Dz} \hat{z})$  represents the drag force per unit volume in the fluid phase. Since the particle transport system considers the particle parameter values at the two nodes within the control volume (explained in section 2.2), the equivalent values of these parameters,  $\rho_p$  and  $\vec{U}_p$ , should be considered for the drag calculation in the fluid phase. Assuming very low particle  $Re_p$ , Stokes drag has been considered here,  $\vec{F}_D = 3\pi\mu d_p (\vec{U} - \vec{U}_p) \frac{\rho_p}{m_p}$ .  $m_p$  is the mass of a single particle.  $E_D$  is the energy transfer rate due to drag force between the two phases and is given by  $E_D = \vec{F}_D \cdot \vec{U}_p$ .  $\tau$  represents the viscous stress tensor, and  $q$  represents the energy generation due to fluid viscous forces and heat diffusion.

### 2.2. Particle moment transport equations

The conventional transport method for Eulerian particles averages out particle velocities, which can nullify the reflective effect of the wall. Additionally, this method may average out the distinct velocities of particles within the control volume, leading to inaccuracies in cases involving inter-particle collisions, trajectory-crossing, and dispersion. Furthermore, the absence of a pressure term in the transport equations can cause ill-posedness in the system (Bouchut 1994). This pressureless gas dynamics approach can result in an overestimation of particle number density in low-speed streaks of turbulent flows (Desjardins *et al.* 2008).

To improve the accuracy of the simulations, a two-node quadrature-based moment method, as proposed by Desjardins *et al.* (2006, 2008), is employed in the present study. The use of two nodes prevents complete averaging of the velocity field and retains the reflected velocity of the particles at the wall, thereby accurately capturing particle-wall interactions. This method has also been shown to accurately capture particle clustering in turbulent flows. Additionally, the study considers transport equations for moments up to the third order, enhancing the method's ability to effectively capture particle trajectory-crossing within the control volume (Fox 2012; Baker *et al.* 2020). Since the quadrature method accounts for velocities at two distinct nodes within the control volume, it is also a promising approach for simulating high Mach number flows while avoiding numerical instabilities and negative weights (Fox 2012). For a non-evaporating, monodispersed particle phase with no interparticle collisions, turbulent dispersion, or atomization, the quadrature-based moment method can be derived from the Williams equation (Williams 1958),

$$\frac{\partial f}{\partial t} + \vec{\nabla}_E \cdot (f \vec{V}_p) + \vec{\nabla}_v \cdot \left( f \frac{\vec{F}_D}{m_p} \right) = 0.$$

Here,  $f$  represents the number density function,  $\vec{\nabla}_E$  represents the normal gradient in the Euclidean space, and  $\vec{\nabla}_v$  represents the gradient in the velocity space. Since the particle density is considered to be much higher than that of fluid density, only drag force is considered to be acting on the particle.

The quadrature-based moment method solves the system of equations that conserves up to the third-order moment of velocities within the control volume. For small Stokes numbers, these moments can be approximated using the particle parameters at two nodes.

$$\begin{aligned} 0^{th} \text{ order moment: } M^0 &= \rho_{p1} + \rho_{p2} \\ 1^{st} \text{ order moment: } M_i^1 &= \rho_{p1} U_{p1i} + \rho_{p2} U_{p2i} \\ 2^{nd} \text{ order moment: } M_{ij}^2 &= \rho_{p1} U_{p1i} U_{p1j} + \rho_{p2} U_{p2i} U_{p2j} \\ 3^{rd} \text{ order moment: } M_{ijk}^3 &= \rho_{p1} U_{p1i} U_{p1j} U_{p1k} + \rho_{p2} U_{p2i} U_{p2j} U_{p2k} \\ 3^{rd} \text{ order moment: } Q &= \rho_{p1} \sum_{x,y,z} U_{p1}^3 + \rho_{p2} \sum_{x,y,z} U_{p2}^3 \end{aligned}$$

Here,  $i, j, k$  represent the three directions.  $U_{p1}$  &  $U_{p2}$  are the particle velocities at node 1 and node 2, respectively. Similarly,  $\rho_{p1}$  &  $\rho_{p2}$ , being different from the material density of the particles, represent the particle equivalent densities at the two nodes within the control volume. Using these definitions of the moments, the moment transport equations

for a three-dimensional particle flow can be formulated as:

$$\begin{aligned}
\frac{\partial M^0}{\partial t} + \vec{\nabla} \cdot (M_x^1 \hat{x} + M_y^1 \hat{y} + M_z^1 \hat{z}) &= 0 \\
\frac{\partial M_x^1}{\partial t} + \vec{\nabla} \cdot (M_{xx}^2 \hat{x} + M_{xy}^2 \hat{y} + M_{xz}^2 \hat{z}) &= \frac{\rho_{p1}}{m_p} F_{Dx1} + \frac{\rho_{p2}}{m_p} F_{Dx2} \\
\frac{\partial M_y^1}{\partial t} + \vec{\nabla} \cdot (M_{yx}^2 \hat{x} + M_{yy}^2 \hat{y} + M_{yz}^2 \hat{z}) &= \frac{\rho_{p1}}{m_p} F_{Dy1} + \frac{\rho_{p2}}{m_p} F_{Dy2} \\
\frac{\partial M_z^1}{\partial t} + \vec{\nabla} \cdot (M_{zx}^2 \hat{x} + M_{zy}^2 \hat{y} + M_{zz}^2 \hat{z}) &= \frac{\rho_{p1}}{m_p} F_{Dz1} + \frac{\rho_{p2}}{m_p} F_{Dz2} \\
\frac{\partial M_{xx}^2}{\partial t} + \vec{\nabla} \cdot (M_{xxx}^3 \hat{x} + M_{xxy}^3 \hat{y} + M_{xxz}^3 \hat{z}) &= 2 \frac{\rho_{p1}}{m_p} u_{p1} F_{Dx1} + 2 \frac{\rho_{p2}}{m_p} u_{p2} F_{Dx2} \\
\frac{\partial M_{yy}^2}{\partial t} + \vec{\nabla} \cdot (M_{yyx}^3 \hat{x} + M_{yyy}^3 \hat{y} + M_{yyz}^3 \hat{z}) &= 2 \frac{\rho_{p1}}{m_p} v_{p1} F_{Dy1} + 2 \frac{\rho_{p2}}{m_p} v_{p2} F_{Dy2} \\
\frac{\partial M_{zz}^2}{\partial t} + \vec{\nabla} \cdot (M_{zzx}^3 \hat{x} + M_{zzy}^3 \hat{y} + M_{zzz}^3 \hat{z}) &= 2 \frac{\rho_{p1}}{m_p} w_{p1} F_{Dz1} + 2 \frac{\rho_{p2}}{m_p} w_{p2} F_{Dz2} \\
\frac{\partial Q}{\partial t} + \vec{\nabla} \cdot (R_x \hat{x} + R_y \hat{y} + R_z \hat{z}) &= 3 \frac{\rho_{p1}}{m_p} \sum_{x,y,z} (U_{p1}^2 F_{D1}) + 3 \frac{\rho_{p2}}{m_p} \sum_{x,y,z} (U_{p2}^2 F_{D2})
\end{aligned} \tag{2.2}$$

$\vec{F}_{D1} = F_{Dx1} \hat{x} + F_{Dy1} \hat{y} + F_{Dz1} \hat{z}$  and  $\vec{F}_{D2} = F_{Dx2} \hat{x} + F_{Dy2} \hat{y} + F_{Dz2} \hat{z}$  represent the drag forces between the fluid and the particle field, at the two nodes. At the  $n^{th}$  node,  $\vec{F}_{Dn} = 3\pi\mu d_p(\vec{U} - \vec{U}_{pn})$ . The last equation in the system represents the transport equation for the  $3^{rd}$  order moment  $Q$  with  $\vec{R} = R_x \hat{x} + R_y \hat{y} + R_z \hat{z}$  being the closure required for the system.

In the  $i^{th}$  direction, the value of  $R$  reads  $R_i = \rho_{p1} \left( \sum_{x,y,z} U_{p1}^3 \right) U_{p1i} + \rho_{p2} \left( \sum_{x,y,z} U_{p2}^3 \right) U_{p2i}$ .

By solving the above system, the values of particle velocities and their equivalent densities at the two nodes can be evaluated within the control volume. Using these values, equivalent values of particle velocity and equivalent density are calculated as  $\rho_p = M^0$ ,  $u_p = M_x^1/M^0$ ,  $v_p = M_y^1/M^0$ , and  $w_p = M_z^1/M^0$ .

### 2.3. Numerical method

The set of equations in the system 2.1 and 2.2 can be summarized as

$$\frac{\partial C}{\partial t} + \vec{\nabla} \cdot \vec{F} = \vec{\nabla} \cdot \vec{\bar{S}}_v + S_c.$$

For a control volume  $\Delta\mathcal{V}$ , the system can be written as

$$\frac{\partial C}{\partial t} \Delta\mathcal{V} + \vec{F} \cdot d\vec{s} = \vec{\bar{S}}_v \cdot d\vec{s} + S_c \Delta\mathcal{V}, \tag{2.3}$$

where  $C$  represents the conservative variable,  $\vec{F} \cdot d\vec{s}$  is the flux of convective variables,  $\vec{\bar{S}}_v$  is the viscous source term in the fluid transport equation, and  $S_c$  represents the interphase coupling source term. The matrices representing these variables are detailed in appendix A.

The numerical method is similar to that described by Desjardins *et al.* (2008), where they considered a fractional two-step approach to solve the particle moment equations. The approach has been extended to solve the fluid transport equations in the present work. In the first step, transport equations of both phases described by the system 2.3



are solved without the coupling source terms  $S_c$  to get the approximate values of the conservative variables  $C_f^*$  and  $C_p^*$  after the time step  $\Delta t$ . A Runge-Kutta type integration method is used to calculate  $C_f^*$  and  $C_p^*$ . In the second step, the system 2.3 is solved without  $\vec{F}$  and  $S_v$ , using the values approximated in the first step, to get new values of the conservative variables  $C^{**}$ .

To increase the temporal accuracy of the solution to second order, the mid-time-step values are estimated by calculating the mean values of  $C^{**}$ , calculated after the time step  $\Delta t$ , and  $C$ , from the previous time step. Using the mid-time-step values and the previous time values, the fractional two-step approach is repeated to calculate the final values of the conservative variables that are second-order accurate in time. Further details on the calculation of particle transport variables at the two nodes are given by Desjardins *et al.* (2006, 2008).

The flux of the fluid convective variables  $\vec{F}_f \cdot d\vec{s}$  is calculated explicitly using the Simple Low dissipation [Advection Upstream Splitting Method (AUSM)] scheme (SLAU2) (Kitamura & Shima 2013, 2010). The scheme belongs to the AUSM family of schemes that were originally developed to simulate high-speed flows and have since been modified over the years to simulate both high and low-speed flows (Liou & Steffen Jr 1993; Liou 1996, 2006; Shima & Kitamura 2011; Shima 2013; Chen *et al.* 2020). For the present simulation, the scheme is converted to second order in space by interpolating the fluid parameters at the cell face using the least square method (Björck 1996) and Venkatakrishnan limiter (Venkatakrishnan 1993, 1995). The same least square method is also used to evaluate the viscous source terms  $S_v$ . As an upwind scheme, SLAU2 can be overly dissipative for low Mach number flows (Thornber *et al.* 2008b). The dissipation rate increases as the inverse of the Mach number,  $M$  (Thornber *et al.* 2008a). Thus, in the incompressible regime, for  $M < 0.3$ , a significant dissipation of the solution can be expected. To deal with this inherent dissipation of the scheme, a velocity correction proposed by Thornber *et al.* (2008b) is implemented. The correction method was applied by Kokkinakis (2009) in the simulation of a turbulent channel flow at  $M = 0.2$  using the upwind Harten, Leer, Lax Contact (HLLC) scheme (Toro *et al.* 1994; Toro 2019). The correction significantly reduced the dissipation on coarser grids. Matsuyama (2014) demonstrated the effectiveness of the correction in reducing the dissipation in his DNS simulation of a low Mach number channel flow using various upwind schemes, including SLAU (predecessor of SLAU2) (Shima & Kitamura 2011). According to the correction, the velocity values extrapolated to the left and right of the cell face ( $U_l$  &  $U_r$ ) are adjusted using the minimum value of local interface Mach number ( $M_l$  &  $M_r$ ):

$$U_l^{LM} = \frac{U_l + U_r}{2} + Z \frac{U_l - U_r}{2}; \quad U_r^{LM} = \frac{U_l + U_r}{2} - Z \frac{U_l - U_r}{2}$$

$$Z = \min[1, \max(M_l, M_r)]$$

This adjustment of the velocities is incorporated after the calculation of the mass flux and the pressure flux at the cell face. The adjustment reduces the sharp changes in the left and right values of the velocities, which contribute to the dissipation. We find that using the absolute values of the local Mach numbers to calculate  $Z$  gives the best results. As will be shown in section 4.1, the correction significantly improved the results in low Mach number flow when the fluid is in an incompressible regime. At high Mach number flows,  $Z$  takes the value of unity, thus retaining the original scheme.

The flux of the particle convective variables  $\vec{F}_p \cdot d\vec{s}$  are calculated using an upwind type flux splitting method described by Desjardins *et al.* (2006, 2008). The method is based on the kinetic schemes (Pullin 1980; Deshpande 1986; Perthame 1992;



Estivalezes & Villedieu 1996). The scheme is converted to  $2^{nd}$  order in space by interpolating all the convective variables at the cell boundary in a similar fashion as done for the fluid.

The whole methodology is developed in CUDA (Sanders 2010; Cook 2012) to implement GPU parallelization, which significantly reduces the computation time. The computations are carried out using A100 Graphical Processor Units in a DGX cluster.

### 3. Flow parameters and configuration

The particle volume fraction  $\phi_v$ , the total volume of particles per unit volume of the fluid, and particle mass loading  $\phi_m$ , defined as the ratio between total particle mass in the channel and the total fluid mass, determine the type of interactions between the two phases (Balachandar & Eaton 2010b; Kasbaoui 2019). At the limit of low values of  $\phi_v$  and  $\phi_m$ , the particles act as passive tracers, hardly affecting the flow or other particles. At higher values of  $\phi_v$  ( $> 10^{-3}$ ) and  $\phi_m O(1)$ , both particle-fluid and particle-particle interactions are significant. When  $10^{-6} < \phi_v < 10^{-3}$ , particle-particle interactions become secondary or negligible, and particle-fluid interactions dominate. The nature of particle-fluid interactions is determined by the Stokes number  $St$ . Since two-way coupling is considered in the present work, the flow configuration parameters for the two phases are chosen in such a way that ensures the presence of fluid-particle interactions but justifies the omission of the particle-particle interactions.

Monodisperse particle-laden channel flows are considered for the study. Two different frictional Stokes numbers  $St^+$  are studied; where  $St^+ = \tau_p u_\tau^2 / \nu$  is based on the frictional time scale of the flow. Here,  $\tau_p$  is the particle time scale,  $u_\tau$  is the frictional velocity ( $u_\tau = Re_\tau * \nu / h$ ), and  $\nu$  represents the kinematic viscosity of the flow. Three different values of  $\phi_m$  are considered for each particle type. These, along with other parameters, are outlined in Table 1. In all cases, the particle size is less than the Kolmogorov length scale of the carrier flow. The number density of particles inside the domain is chosen such that  $\phi_{v0}$  is between  $10^{-5}$  and  $10^{-4}$ , thus ensuring the dominance of the two-way coupling. We also find that even in clustered regions,  $\phi_v$  is always  $< 10^{-3}$ .

For each case, the fluid flow inside the channel has  $Re = 2800$  and  $Re_\tau = 180$ , based on the channel half height. The fluid flow velocity corresponds to  $M = 0.12$ . Thus, the flow can be considered incompressible. By simulating an incompressible fluid flow using a compressible flow solver, we can thus establish the capability of the developed solver to effectively solve the flow in a wide range of Mach numbers. However, it should be mentioned that the solver assumes the fluid to be an ideal gas.

A rectangular channel is used for the simulations. A slightly wider domain is considered for the high  $St^+$  case to capture the increased spanwise spacing of the particles (Dave & Kasbaoui 2023). Although the domain of high  $St^+$  is wider than that of low  $St^+$ , comparing the effects of two particle types is plausible due to the use of periodic boundary conditions in the spanwise direction. The smaller domain for low  $St^+$  case is similar to the domains used by Moser *et al.* (1999) in their DNS of incompressible fluid flow. Dave & Kasbaoui (2023) used a similar domain in their DNS of the particle-laden channel flows with  $St^+ = 6$  using the Lagrangian approach. The larger domain is similar to the one used by Zhao *et al.* (2010) and Zhou *et al.* (2020) in their DNS of the particle-laden channel flows with  $St^+ = 30$  involving Lagrangian particles. Similar domains allow us to effectively compare/validate the results of our simulation employing a compressible fluid solver and the Eulerian particle method. For both domains, the mesh resolution is constant in the streamwise and spanwise directions, with  $\Delta x = 0.048h$  and  $\Delta z = 0.032h$ .

Table 1: Table representing the non-dimensional parameters for particle-laden turbulent channel flows.  $\rho_{pp}$  and  $\rho$  are the density of the particle material and fluid, respectively.  $\phi_{v0}$  is the initial volume fraction of particles when they are introduced uniformly in the channel. The channel dimensions in the streamwise, wall-normal, and spanwise directions are  $l_x$ ,  $l_y$ , and  $l_z$  respectively.

$St^+$	$\phi_m$	$l_x/h$	$l_y/h$	$l_z/h$	$d_p/h$	$\rho_{pp}/\rho$	$\phi_{v0}(\times 10^{-5})$
6	0.2	$4\pi$	2	$(4/3)\pi$	0.0005	13697	1.46
6	0.6	$4\pi$	2	$(4/3)\pi$	0.0005	13697	4.38
6	1.0	$4\pi$	2	$(4/3)\pi$	0.0005	13697	7.08
30	0.2	12	2	6	0.0011	13697	1.45
30	0.6	12	2	6	0.0011	13697	4.37
30	1.0	12	2	6	0.0011	13697	7.05

In the wall-normal direction, the mesh is refined smoothly from the channel center, where  $\Delta y = 0.028h$ , towards the wall, where  $\Delta y = 0.0036h$  results in a  $y^+ = 0.65$ .

Periodic boundary conditions are applied in the streamwise and spanwise directions for both phases. A no-slip condition is imposed on the fluid at the wall. Elastic reflection condition for particles at the wall is defined by balancing the inflow and outflow of particle flux, ensuring no net exchange of mass or tangential particle momentum through the wall while reversing the normal component of the particle momentum. This type of boundary condition has been utilized by Desjardins *et al.* (2006, 2008) to demonstrate the effectiveness of the quadrature-based moment method in capturing wall reflections of the Eulerian particle phase. A small pressure difference between the inlet and outlet is introduced to balance the wall shear stress caused by viscosity, thus maintaining the flows at  $Re_\tau = 180$ .

The domains are initialized with the fluid phase variables without the particles. Random fluctuations are initially introduced in the three components of velocity to trigger the development of turbulence. These local fluctuations can vary in both magnitude and direction. In the streamwise direction, they can reach up to half the initialized streamwise velocity of the flow. Although the flows are initialized with a zero velocity in the spanwise and wall-normal directions, fluctuations are introduced in these directions also, ranging from  $-1m/s$  to  $1m/s$ . This allows for the development of turbulence in all three directions.

The particle-free channel (PFC) flow in each case is then simulated for around 125 eddy turnover time  $\Delta t_\eta (= \frac{h}{u_\tau})$  for the flow to reach a statistically steady state. The flow is further simulated for 30  $\Delta t_\eta$  to record data for the analysis. Subsequently, particles are introduced uniformly into the flow with the flow velocity. Particle-laden channel (PLC) flows are then simulated for 125  $\Delta t_\eta$  to achieve another statistically steady state, after which data are recorded in the same fashion as for the PFC flow.

## 4. Results and discussions

### 4.1. Flow statistics

The PFC flow is used here and in subsequent sections as a baseline reference, which is compared to the PLC flow cases to highlight mean flow and turbulence modulations induced by the particles. As the objective of this study is to expand the capabilities of the Eulerian approach, it is instructive to compare the results to previous studies, most of which focus on the low Mach number regime. To achieve this, we start by assessing the ability of the SLAU2 scheme (second order) to simulate the PFC flow within the incompressible regime.

The SLAU2 scheme is an upwind scheme that can be used to simulate high-speed flows (Kitamura & Shima 2013; Kitamura & Hashimoto 2016; Mamashita *et al.* 2021). Though its ability to simulate low-speed flows has been claimed, it has not been validated for channel flows. Matsuyama (2014) established the validity of its predecessor (SLAU) to simulate low-speed flows. However, the author used up to seventh-order WENO interpolation for the validation. Yet, achieving a 7th-order conversion demands substantial computational resources. The second-order SLAU2 scheme, on the other hand, is expected to be more efficient and computationally less expensive.

Figure 1 illustrates the velocity statistics profiles in a PFC flow with  $Re_\tau = 180$ . Once the flow reaches a statistically steady state, three hundred samples of flow data at various time instances are collected to calculate the mean flow statistics. The time instance of each sample differed from the previous one by  $\frac{\Delta t_\eta}{10}$ . Consequently, averaging is performed over a total time period of  $30\Delta t_\eta$  and across the two homogenous directions to reach convergence of the turbulence statistics. Using the mean values of velocity components, root-mean square (rms) values of the velocity fluctuations are calculated.

Figure 1a shows the variation of the mean streamwise flow velocity  $\bar{u}$  along the channel height. The plots include results from simulations using the second-order SLAU2 scheme, both with and without the Thornber correction, and compare them with previous DNS results by Moser *et al.* (1999) for validation. The results indicate that the SLAU2 scheme with the Thornber correction produces velocity profiles similar to those of Moser *et al.* However, without the correction, the scheme overestimates the averaged velocity in regions away from the wall due to increased dissipation. Thus, it can be concluded that using the Thornber correction can significantly reduce the unwanted dissipation inherent in the SLAU2 scheme and will be used throughout the present study.

Figure 1b shows the variation of velocity rms values in three directions. For clarity, rms values from simulations without the correction are not included in the figure. Together with Figure 1a, these results demonstrate the ability of the second-order SLAU2 scheme with the Thornber correction to accurately simulate the flow within the incompressible regime.

After the framework for clean flow simulations is established for the channel, particles are added to the flow. Upon reaching the new statistically steady state, the averaged flow statistics are calculated in the same manner as done for the PFC flow. The effect of particles on the mean streamwise velocity  $\bar{u}$  is presented in figure 2 for two different Stokes numbers and three different particle mass loadings for each Stokes number. The figure shows that, in all cases, the presence of particles leads to an increase in the mean streamwise velocity.

Dave & Kasbaoui (2023) explained that particles may enhance the flow rate. However, their findings for the PLC flows with  $St^+ = 6$  are in contrast with the present results. While they assumed the particles with semi-dilute conditions,  $\phi_{v0}$  used by them was about one order higher than that used in the present study. Moreover, due to particle

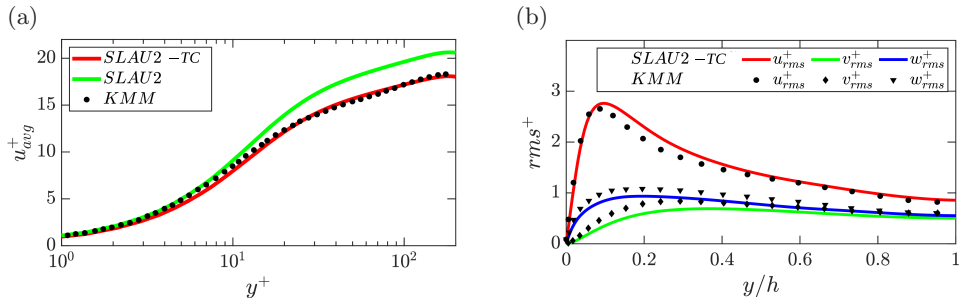


Figure 1: Variation of (a) mean streamwise velocity and (b) RMS of velocity fluctuations along the channel height in a particle-free turbulent channel flow. Results using the upwind SLAU2 scheme with Thornber’s correction are validated against those of Moser *et al.* (1999). Reduction in numerical dissipation using Thornber’s correction can also be noticed.

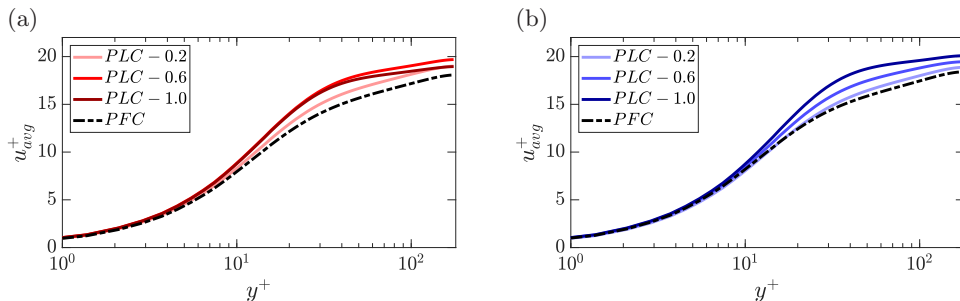


Figure 2: Variation of fluid mean streamwise velocity along the channel height for the PFC flow and different PLC flows with (a)  $St^+ = 6$  and (b)  $St^+ = 30$ . Darker lines correspond to higher particle mass loadings varying from 0.2 to 1.0.

clustering,  $\phi_v$  can increase locally to a high value (Kasbaoui *et al.* 2019). It is plausible that in the study by Dave and Kashbaoui, particles’  $\phi_v$  locally breached the boundary of semi-dilute conditions when inter-particle interactions, which were considered inelastic, become significant. Furthermore, inelastic collisions were considered between the particles and the wall. It was shown by Vreman *et al.* (2009) that inelastic inter-particle interactions and particle-wall collisions can flatten the mean velocity profile as the flow loses energy to inelastic interactions. In contrast, the present study, which considers particles in the dilute conditions ( $\phi_v < 10^{-3}$ ), involves elastic wall-particle collisions and ignores inter-particle collisions, which may result in an increase in the mean flow velocity.

Though the addition of particles increased  $\bar{u}$ , this increment in the fluid mean velocity is affected by  $\phi_m$ . For  $St^+ = 6$ ,  $\bar{u}$  increases as  $\phi_m$  is increased from 0.2 to 0.6. Notably, further increase in  $\phi_m$  to 1.0 reduces  $\bar{u}$ . This is obvious as after a certain limit, an increase in the number of particles will tend to increase the drag and thus will limit the increase in fluid mean velocity. For  $St^+ = 30$ , this effect of  $\phi_m$  is not noticed for the current data set. However, at higher  $\phi_m$ , the same behavior of the particles is expected.

The influence of particles on the flow velocity fluctuations is captured effectively using the Eulerian approach as shown in figure 3. While particles enhance the fluctuations in the streamwise direction, they are attenuated in the transverse directions. Kulick *et al.* (1994)

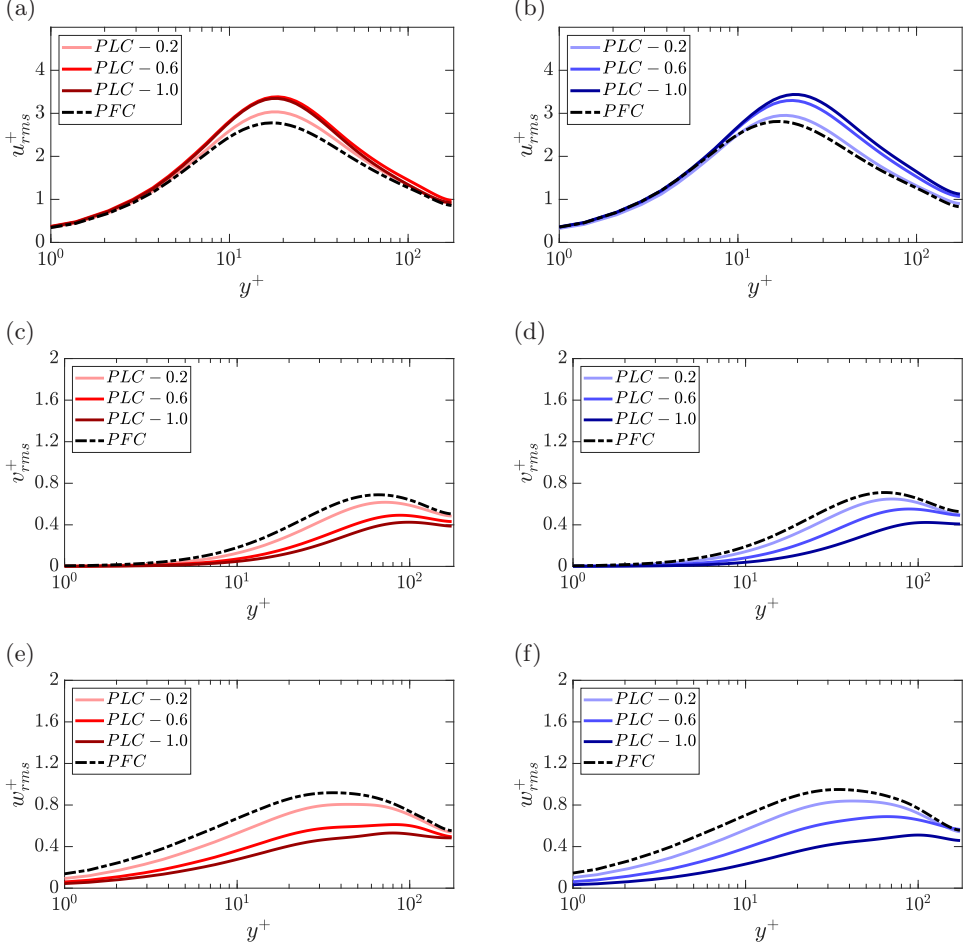


Figure 3: Variation of fluid RMS velocities along the channel height for the PFC flow and different PLC flows with (a, c, e)  $St^+ = 6$  and (b, d, f)  $St^+ = 30$ . Darker lines correspond to higher particle mass loadings varying from 0.2 to 1.0.

reported and explained this anisotropic effect of particles on velocity fluctuations. High frequencies of fluctuations in the transverse directions make it difficult for the inertial particles to adjust to the flow conditions. Thus, the turbulent energy of the transverse fluctuations is dissipated by the particles. With an increase in the number density of particles, more energy in the transverse directions is dissipated. On the other hand, particles adjust to the streamwise fluctuations, which are relatively at lower frequencies and, hence, do not dissipate the turbulent energy. Instead, particles enhance fluctuations in the streamwise direction. However, the current results show that this enhancement in the streamwise velocity fluctuations is affected by the particle  $\phi_m$ , in the same way as the fluid streamwise mean velocity.

With the effect of particles on the flow velocity fluctuations being anisotropic, we find that the addition of particles enhances the overall turbulent kinetic energy ( $TKE$ ) of the flow, as shown in figure 4. For  $St^+ = 6$ , the  $TKE$  increases when  $\phi_m$  is increased from 0.2 to 0.6. However, we notice a decrease in the  $TKE$  upon a further increment of  $\phi_m$

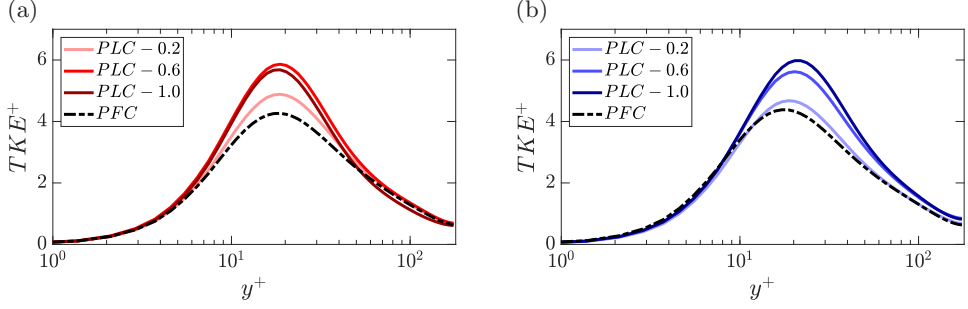


Figure 4: Variation of turbulent kinetic energy along the channel height for the PFC flow and different PLC flows with (a)  $St^+ = 6$  and (b)  $St^+ = 30$ . Darker lines correspond to higher particle mass loadings varying from 0.2 to 1.0.

to 1.0. This can be attributed to the saturation in the  $u_{rms}$  as described in figure 3. For  $St^+ = 30$ , the  $TKE$  increases upon increasing  $\phi_m$ . Squires & Eaton (1994) studied the particle-laden flows with Kolmogorov Stokes number in the range of 0.6 to 6.5, and  $\phi_m$  ranging from 0 to 1.0. They found that for a significant  $\phi_m$ , turbulence structures can get distorted due to preferential clustering of particles, thus reducing the  $TKE$ . They showed that particles tend to increase the dissipation rate due to preferential clustering. Furthermore, Squires & Eaton (1991) reported that the particles with low inertia exhibit a stronger preferential concentration than the particles with high inertia. For the same  $\phi_m = 1.0$ , it can be anticipated that the particles in the flow with  $St^+ = 6$  tend to cluster more than particles in the flow with  $St^+ = 30$  (shown in table 2). More clusters of particles interacting with the turbulence structures finally lead to a reduction in the  $TKE$  for the  $St^+ = 6$  case.

#### 4.2. Total Reynolds shear stress in the flow

The particle's contribution to the total Reynolds shear stress (RSS) in the flow can be modelled by considering the streamwise momentum balance for the statistically steady flow. The flow momentum balance in the streamwise direction gives

$$\frac{\partial(\rho(\bar{u} + u')(\bar{u} + u'))}{\partial x} + \frac{\partial(\rho v'(\bar{u} + u'))}{\partial y} = -\frac{\partial \bar{P}}{\partial x} - \frac{\partial P'}{\partial x} + \mu \frac{\partial^2(\bar{u} + u')}{\partial y^2} - F_{Dx}$$

For a fully developed channel flow, the mean pressure gradient is equal to the wall drag (Pope 2000)

$$\Rightarrow \frac{\partial(\rho v' \bar{u})}{\partial y} + \frac{\partial(\rho u' v')}{\partial y} = \frac{\tau_w}{h} - \frac{\partial P'}{\partial x} + \mu \frac{\partial^2 \bar{u}}{\partial y^2} + \frac{\partial^2 u'}{\partial y^2} - F_{Dx}$$

After averaging over time

$$\Rightarrow \frac{\partial \overline{\rho u' v'}}{\partial y} = \frac{\tau_w}{h} + \mu \frac{\partial^2 \bar{u}}{\partial y^2} - \bar{F}_{Dx} \quad (4.1)$$

Similarly, for particles, the momentum balance in the streamwise direction gives

$$\frac{\partial \overline{\rho_p u'_p v'_p}}{\partial y} = \bar{F}_{Dx} \quad (4.2)$$

Adding Eq. 4.1 to Eq. 4.2,

$$\frac{\partial \overline{\rho u'v'}}{\partial y} + \frac{\partial \overline{\rho_p u'_p v'_p}}{\partial y} = \frac{\tau_w}{h} + \mu \frac{\partial^2 \overline{u}}{\partial y^2}$$

Integrating from  $y$  to  $h$ ,

$$\begin{aligned} -\overline{\rho u'v'} - \overline{\rho_p u'_p v'_p} &= \tau_w \left(1 - \frac{y}{h}\right) - \mu \frac{\partial \overline{u}}{\partial y} \\ \mu \frac{\partial \overline{u}}{\partial y} &= \tau_w \left(1 - \frac{y}{h}\right) - (-\overline{\rho u'v'} - \overline{\rho_p u'_p v'_p}) \end{aligned} \quad (4.3)$$

where  $\tau_w$ , being a function of  $Re_\tau$ , is a constant. While  $-\overline{\rho u'v'}$  gives the fluid RSS,  $-\overline{\rho_p u'_p v'_p}$  is the particle RSS. It can be concluded from Eq. 4.3 that at a particular distance from the wall, the RSS in both phases tends to reduce the viscous stress by reducing the mean streamwise velocity gradient. The less the RSS, the more the streamwise velocity gradient. Particles' effect on the RSS in both phases is shown in figure 5. The addition of particles reduces the fluid RSS, and the reduction increases monotonically with the increase in particle mass loading  $\phi_m$ . This reduction in the RSS can be attributable to the dissipation in fluid velocity fluctuations in wall-normal direction as shown in figure 3. Furthermore, slightly higher values of the fluid RSS can be observed for  $St^+ = 30$  cases than that for  $St^+ = 6$  cases.

The particle RSS increases with an increase in  $\phi_m$ . From Eq. 4.2, it can be interpreted that the particle RSS is a depiction of the mean drag between the two phases. Figure 6 shows the variation of this mean drag force along the channel height. Near the walls, the particle velocity is greater than that of the fluid, resulting in a negative drag. The higher particle velocity at the wall can be attributed to the slip and reflective nature of particle-wall interactions as opposed to the no-slip condition of the fluid phase. Away from the wall, the fluid eventually gains momentum under the effect of pressure gradient and decreased wall effects, resulting in a higher velocity than that of the particle phase. This causes a positive mean drag. The effect of particle mass loading  $\phi_m$  is clear from the figure; as  $\phi_m$  increases, more particles drag the fluid, resulting in an enhancement in both the positive and negative drags. As a result, the particle RSS increases with an increase in  $\phi_m$ , as shown in figures 5c and 5d.

Figure 6 also shows that the distance from the center at which the drag switches from positive to negative decreases with an increase in  $\phi_m$ . This effect is emphasized for  $St^+ = 30$  cases. The mean streamwise drag per unit volume can be formulated as:

$$\overline{F_{Dx}} = \frac{18\mu}{d_p^2} (u - u_p) \phi_v = \frac{\rho_{pp} Re_\tau^2 \mu}{h^2 \rho} \frac{(u - u_p) \phi_v}{St^+} \quad (4.4)$$

$\frac{\rho_{pp} Re_\tau^2 \mu}{h^2 \rho}$  is a constant here in all the cases. Thus, the drag between the two phases is directly proportional to the particle volume fraction and inversely proportional to the Stokes number. For the same  $St^+$ , a higher  $\phi_m$  results in a higher  $\phi_v$  near the channel center (as discussed in section 4.3), which indicates a higher particle number density near the channel center. As more particles drag the fluid when the  $\phi_m$  is higher, the fluid and the particles have more likelihood of attaining equal velocities. Hence, the drag switching takes place at a closer distance from the center when  $\phi_m$  is higher.

The effect of particles' inertia on the drag can be analyzed by comparing the two subfigures in figure 6. For clarity, this comparison at  $\phi_m = 0.6$  is shown in figure 7. Near the channel center, the drag between the low inertia particles ( $St^+ = 6$ ) and the



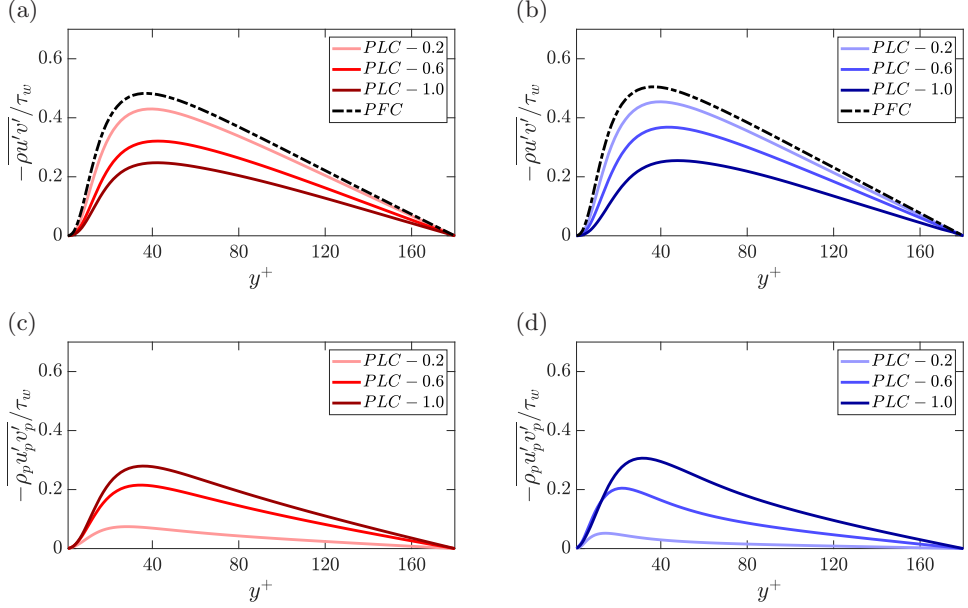


Figure 5: Variation of different Reynolds shear stress along the channel height. The fluid Reynolds shear stress in the PFC flow and different PLC flows are shown in (a) for  $St^+ = 6$  and (b) for  $St^+ = 30$ , while the particle Reynolds shear stress in different PLC flows are shown in (c) for  $St^+ = 6$  and (d) for  $St^+ = 30$ . Darker lines correspond to higher particle mass loadings varying from 0.2 to 1.0.

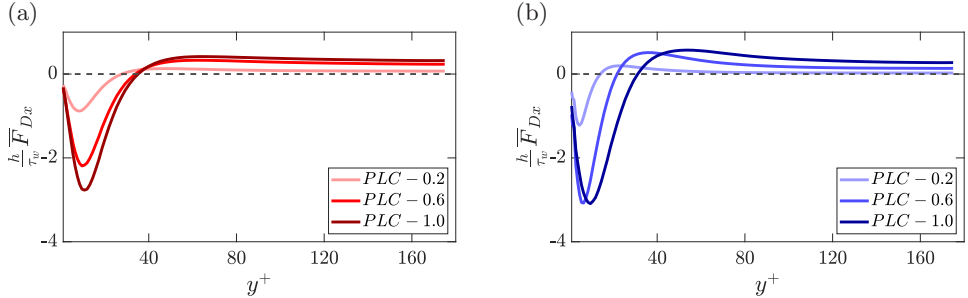


Figure 6: Variation of mean drag  $\left( \frac{\partial \rho_p u'_p v'_p}{\partial y} \right)$  between the fluid phase and the particle phase along the channel height for different PLC flows with (a)  $St^+ = 6$  and (b)  $St^+ = 30$ . Darker lines correspond to higher particle mass loadings varying from 0.2 to 1.0. The dashed line separates the positive and negative drag.

fluid is slightly more than that between the high inertia particles ( $St^+ = 30$ ) and the fluid. As discussed in section 4.3, low inertia particles exhibit higher  $\phi_v$  near the channel center than high inertia particles (for the same  $\phi_m$ ). Therefore, following Eq. 4.4, a higher positive drag in the PLC flow with  $St^+ = 6$  than in the PLC flow with  $St^+ = 30$  can be concluded near the channel center. Furthermore, due to higher drag by low inertia particles, the drag profile switches sign at a closer distance from the channel center when  $St^+ = 6$  than when  $St^+ = 30$ . Near the wall, high inertia particles exhibit a higher  $\phi_v$ ,

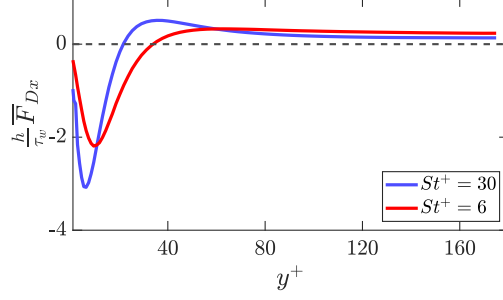


Figure 7: Comparison of fluid-particle drag between the flows with  $St^+ = 6$  and  $St^+ = 30$ , at the same  $\phi_m = 0.6$ . The dashed line separates the positive and negative drag.

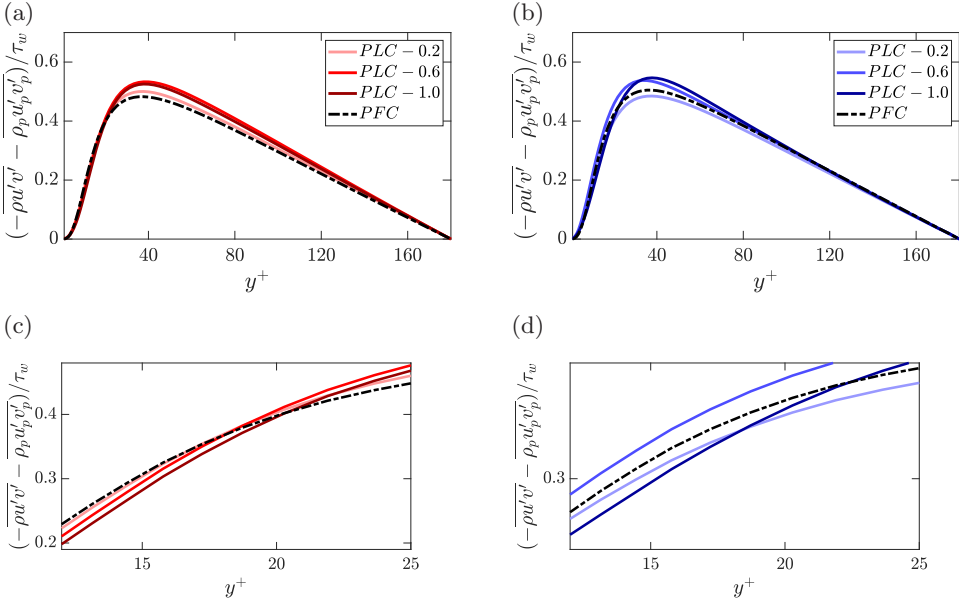


Figure 8: Variation of total Reynolds shear stress in the PFC flow and different PLC flows with (a and c)  $St^+ = 6$  and (b and d)  $St^+ = 30$ . (c and d) shows the trend reversal of this stress in the region of  $y^+ = 20$ . Darker lines correspond to higher particle mass loadings varying from 0.2 to 1.0.

resulting in a larger negative drag. Similar trends are observed for other values of  $\phi_m$ . Thus, it can be concluded that particles with high inertia impose a greater negative drag closer to the wall, while low inertia particles impose a greater positive drag away from the wall. This varying effect of particle inertia on drag along the channel height suggests that the relationship between the particle RSS and  $St^+$  may not be uniform along the channel height. This behavior is consistent with observations from previous studies (Zhao *et al.* 2010; Zhou *et al.* 2020; Dave & Kasbaoui 2023) that used the Lagrangian method for particle tracking.

The effect of particles on the total RSS in both phases is represented in figure 8. There is no substantial effect of particles on the total RSS in the region very close to the wall and to the channel center, where the total RSS remains almost equal to the RSS in the

PFC flow. In the region from  $y^+ = 20$  to  $y^+ = 100$ , the total RSS increases to more than that in the PFC flow when low inertia particles are added. At the lowest  $\phi_m = 0.2$ , the increment is low but is significantly high when  $\phi_m$  increases to 0.6. However, further increment in  $\phi_m$  to 1.0 causes a reduction in the total RSS. For  $St^+ = 30$ , the total RSS in this region is lower than that in the PFC flow when  $\phi_m = 0.2$ , while it is higher than that in the PFC flow at higher mass loadings.

A trend reversal can be noticed in the region with  $y^+ < 20$  (shown in figures 8 c & d) where the total RSS in the PLC flows is less than that in the PFC flow at all values of  $\phi_m$  for  $St^+ = 6$ , and at  $\phi_m = 0.2$  and 1.0 for  $St^+ = 30$ . For these cases, a lower value of the total RSS can also be noticed at a higher  $\phi_m$ . At  $\phi_m = 0.6$  and  $St^+ = 30$  PLC flow, the total RSS is always higher than that in the PFC flow.

#### 4.3. Near-wall particle accumulation and preferential clustering

Particle migration toward the wall and their clustering in a wall-normal plane of a turbulent channel flow at any time instance can be quantified by comparing the instantaneous particle volume fraction  $\phi_v$  with their initial volume fraction  $\phi_{v0}$  when the particle distribution is uniform throughout the channel. This is demonstrated in figure 9 that shows instantaneous contour plots of  $\phi_v$ , normalized by  $\phi_{v0}$ , in a wall-normal plane at the channel center. All subfigures demonstrate the capability of the present Eulerian method to capture the intricate particle field, showing the streaks of particles elongated in the streamwise direction. Streaks in flows with  $St^+ = 30$  are longer and more intense than in flows with  $St^+ = 6$ . In all the cases, particles' tendency to migrate and accumulate near the wall can be noticed.

This phenomenon is demonstrated in figure 10, which shows the variation of the time-averaged values of the normalized  $\phi_v$  along the channel height. It can be seen that relative to the initial volume fraction, the particle accumulation at the wall decreases with an increase in  $\phi_m$ . As a result of the conservation of the total number of particles in the channel, the void density near the channel center is higher at lower  $\phi_m$ s. high inertia particles in PLC flows with  $St^+ = 30$  tend to have a greater near-wall accumulation than low inertia particles in the PLC flows with  $St^+ = 6$ . As illustrated in table 1, at a particular  $\phi_m$ , the initial volume fraction is similar for each particle type. This means the low inertia particles have a higher number density in the channel than high inertia particles. Consequently, flows with  $St^+ = 30$  have higher voids at the channel center than flows with  $St^+ = 6$ . These observations are similar to those obtained by the Lagrangian approach (Dave & Kasbaoui 2023).

Previous studies have attributed this phenomenon of particle accumulation near the wall to the particles' inertia, due to which the particles migrate to low turbulence regions by the effect of turbophoresis (Reeks 1983; Kuerten *et al.* 2011; Nowbahar *et al.* 2013; Johnson *et al.* 2020). Near-wall accumulation of the particles and the presence of particle voids away from the wall affect the drag between the two phases which ultimately affects the total RSS in the flow as discussed in section 4.2.

The particles not only accumulate near the wall but can also preferentially cluster along the velocity streaks in the near-wall region (Eaton & Fessler 1994; Squires & Eaton 1994; Marchioli & Soldati 2002; Kasbaoui *et al.* 2019; Berk & Coletti 2023). Sardina *et al.* (2012) showed that turbophoresis and preferential clustering of particles occur simultaneously in wall-bounded flows. The phenomenon of preferential clustering in the low-speed streaks was observed to be more dominant for smaller particles (Eaton & Fessler 1994; Squires & Eaton 1991), while larger particles could accumulate in either low-speed streaks (LSS) or high-speed streaks (HSS) (Peng *et al.* 2024). Using

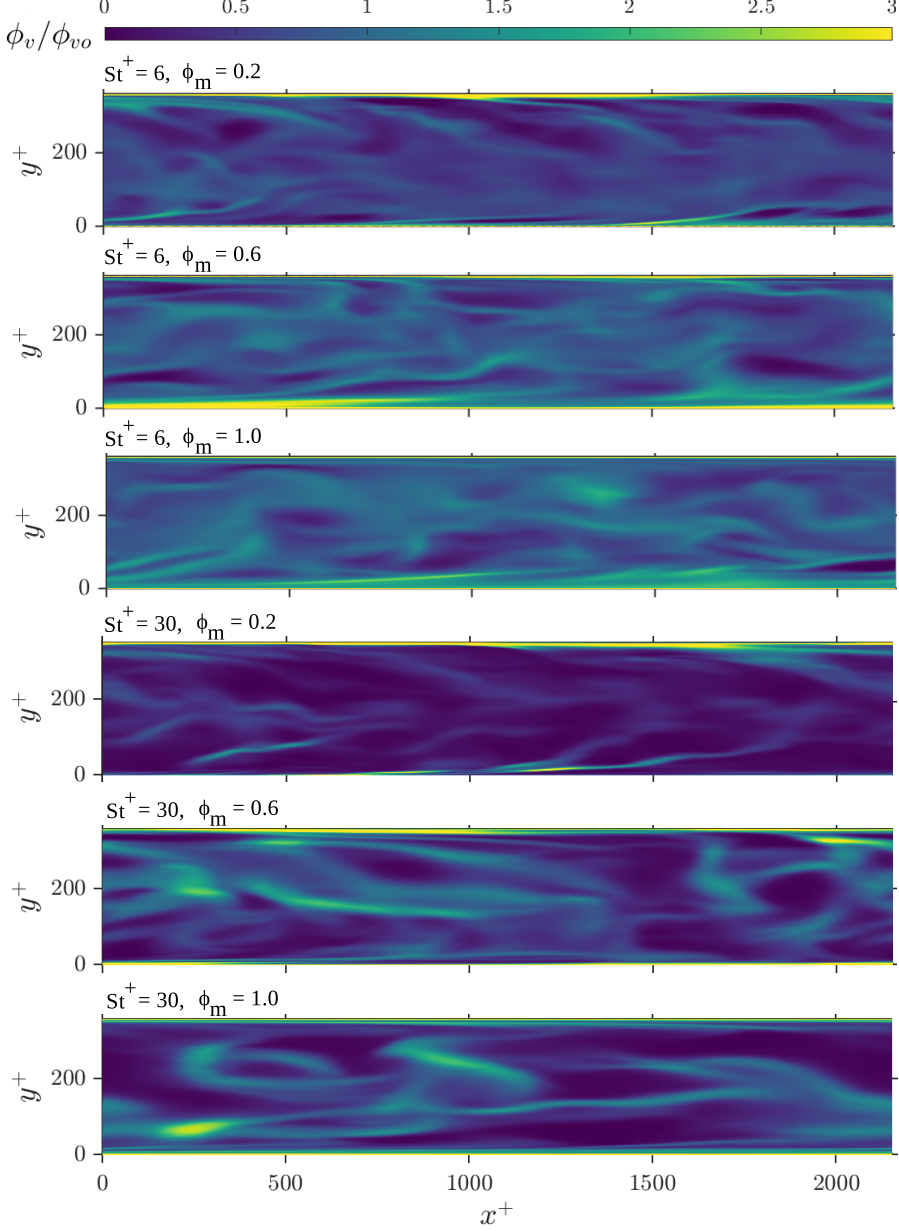


Figure 9: Contour plots of instantaneous particle volume fraction, normalized by the initial volume fraction, in the wall-normal plane, for different combinations of  $St^+$  and  $\phi_m$ . The plots show particle streaks aligned in the streamwise direction. High values of  $\phi_v/\phi_{v0}$  in the near-wall regions indicate particle accumulation.

the present Eulerian approach for the particle field, we found the preferential clustering of both types of particles in LSS.

For  $St^+ = 6$ , the best negative correlation is obtained near  $Y^+ = 15$ , while for  $St^+ = 30$ , it is obtained in the region near  $Y^+ = 10$ . At the same time instants, figure 12 maps

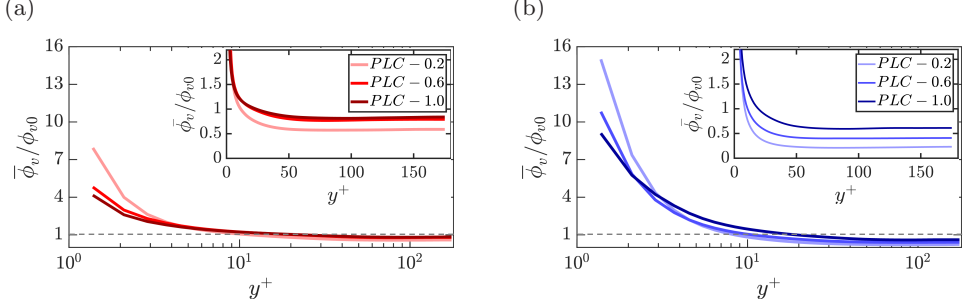


Figure 10: Variation of mean particle volume fraction along the channel height for different PLC flows with (a)  $St^+ = 6$  and (b)  $St^+ = 30$ . The inset compares the particle volume fraction near the channel center for different particle mass loadings. The dashed line represents the reference initial particle volume fraction. Darker lines correspond to higher particle mass loadings varying from 0.2 to 1.0.

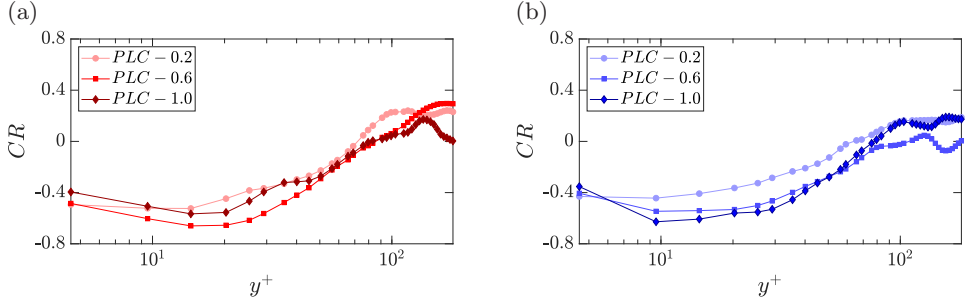


Figure 11: Pearson correlation coefficient between the instantaneous particle volume fraction and the instantaneous streamwise velocity fluctuations in spanwise planes at different  $y^+$  for different PLC flows with (a)  $St^+ = 6$  and (b)  $St^+ = 30$ . Darker lines correspond to higher particle mass loadings varying from 0.2 to 1.0.

the particle volume fraction  $\phi_v$  to the streamwise velocity fluctuations in the near-wall spanwise plane with the most negative correlation and compares it with that in the plane away from the wall ( $y^+ \approx 180$ ), at the lowest particle mass loading  $\phi_m = 0.2$ . It can be seen that for both types of particles, preferential clustering is significant in the near-wall region, with more particles mapping the negative velocity fluctuations than the positive ones. Away from the wall, particles do not show any significant preference toward any type of velocity fluctuations. Thus, it can be concluded that the preferential clustering of particles is a near-wall phenomenon.

Near the wall, different scales of LSS can be present. The particles' preference towards different scales of LSS can be explained using the clustering probability calculated for different sets of velocity streaks. A velocity streak set contains the bounded values of streamwise velocity fluctuations  $u'^+$ . If a specific location in the plane has a velocity streak corresponding to a particular set, clustering probability determines the probability of particle clustering at that location for the corresponding set. We consider clustering at a particular location when  $\phi_v$  at that location is greater than the planar average  $\bar{\phi}_{vp}$ . Thus, the clustering probability for a particular streak set  $V$  at a location in the plane

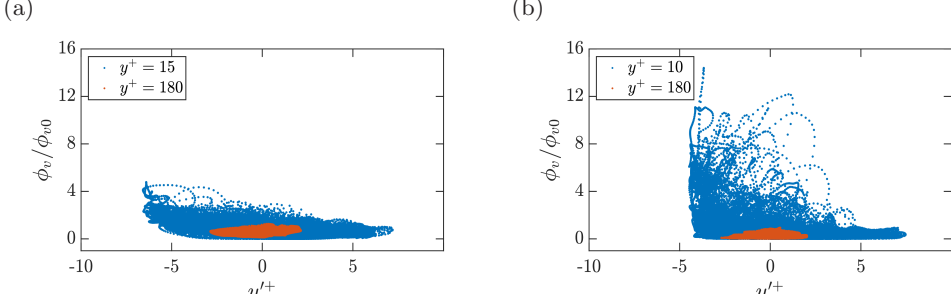


Figure 11 plots the linear correlation between the instantaneous particle volume fraction and the streamwise velocity fluctuations in various spanwise planes along the channel height, calculated using the Pearson correlation coefficient. For both types of particles, a negative correlation is observed near the wall. This signifies that particles near the wall prefer to cluster in the region of LSS. However, it is difficult to effectively predict the correlation away from the wall because of very low particle volume fraction.

Figure 12: Normalized particle volume fraction at different values of streamwise velocity fluctuations in two planes of the PLC flow with (a)  $St^+ = 6$  and (b)  $St^+ = 30$ . The near-wall plane is at the lower  $y^+$  where the correlation shown in figure 11 is most negative, and the plane at the channel center is at  $y^+ \approx 180$ . Both the flows have particle mass loading of 0.2.

is calculated as:

$$P[(\phi_v > \bar{\phi}_{vp})|(u' \in V)] = \frac{P[(\phi_v > \bar{\phi}_{vp}) \cap (u' \in V)]}{P[u' \in V]}$$

At the same time instants, as in figure 11, we find that the instantaneous  $u'^+$  varies from -8 to 8. These fluctuations are divided into eight streak sets, with each being determined by its mean value,  $[-8, -6]$ ,  $[-6, -4]$ ,  $[-4, -2]$ ,  $[-2, 0]$ ,  $[0, 2]$ ,  $[2, 4]$ ,  $[4, 6]$ ,  $[6, 8]$ . The calculated clustering probabilities in the near-wall plane are presented in figure 13. It is clear that for both types of particles for different mass loadings, clustering is strongest in the most negative streaks. In the regions of weak LSS, the probability of particle clustering decreases. The probability of finding particle clusters in HSS is relatively very low. Though particle clustering in LSS is observed in all the cases, the comparison of clustering intensity in different cases illustrates a complex picture (Squires & Eaton 1994).

It may happen that for a particular case, the value of  $\phi_v$  is high at certain locations, but the other case may have more locations with a lower value of  $\phi_v$  (but greater than  $\bar{\phi}_{vp}$ ). By comparing the fraction of the planar area at which  $\phi_v > \bar{\phi}_{vp}$ , an attempt has been made to compare particle clustering for different cases. This gives us the probability of finding the particle clusters in the area. The probability values are tabulated in table 2. The table shows that for  $St^+ = 30$ , the probability of finding the particle clusters increases with  $\phi_m$ , while for  $St^+ = 6$ ,  $\phi_m$  has less effect on the clustering of particles. However, the probability for  $St^+ = 6$  is always higher than that for  $St^+ = 30$ . Thus, it can be concluded that low inertia particles exhibit more clustering than high inertia particles. This is consistent with the notion that particles of high inertia are less responsive to velocity fluctuations and, thus, exhibit less clustering. Clusters can interact with the turbulence structures to increase turbulence dissipation. Thus, a relatively larger number of clusters in the PLC flow with  $St^+ = 6$  and  $\phi_m = 1.0$  may indicate the reason for the decrease in  $TKE$  as discussed in section 4.1.

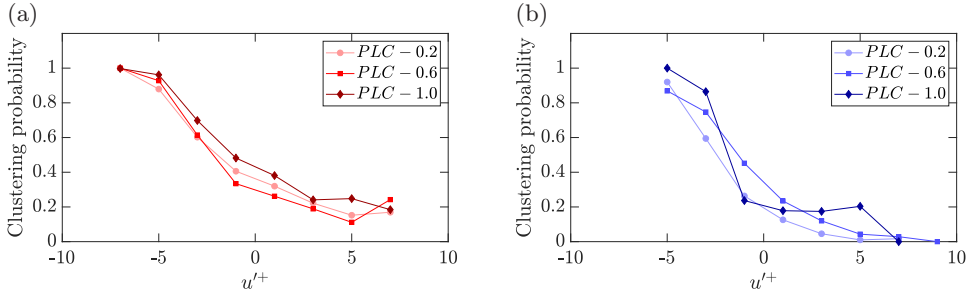


Figure 13: Instantaneous particle clustering probability in the near-wall plane for different values of streamwise velocity fluctuations in the PLC flows with (a)  $St^+ = 6$  where the considered near-wall plane is at  $y^+ \approx 15$  and (b)  $St^+ = 30$  where the considered near-wall plane is at  $y^+ \approx 10$ . Instantaneous data at the same time instants as in figure 11 is analyzed. Darker symbols correspond to higher particle mass loadings varying from 0.2 to 1.0.

Table 2: Instantaneous probability of finding the particle clusters in the spanwise plane, at  $y^+ \approx 15$  for the PLC flows with  $St^+ = 6$  and at  $y^+ \approx 10$  for the PLC flows with  $St^+ = 30$ . Instantaneous data at the same time instants as in figure 11 is analyzed. Particle clusters are considered at any location when the local  $\phi_v > \bar{\phi}_{vp}$ .

$St^+$	$\phi_m = 0.2$	$\phi_m = 0.6$	$\phi_m = 1.0$
6	0.4064	0.3747	0.4097
30	0.2351	0.3238	0.3585

#### 4.4. Particle streaks and turbulence modulation

Particle clusters in LSS can modify the flow turbulence by interacting with the turbulence structures (Squires & Eaton 1990). Zhou *et al.* (2020) showed that the addition of particles to the fluid flow aligns and organizes the velocity streaks. For PLC flows with  $St^+ = 30$ , this is illustrated here in figure 14, which shows the instantaneous contours of streamwise velocity fluctuations in the near-wall spanwise plane at  $y^+ \approx 15$  at the same time instants as figure 11. The contours are overlayed by the red streaks of particles  $\phi_v$ . Values of  $\phi_v > 2.5\bar{\phi}_{vp}$  are shown to illustrate the regions of intense particle clustering. It can be noticed that the addition of particles aligns the turbulence streaks in the streamwise direction. Moreover, fewer streaks that are also more organized and wider than those in the PFC flow are observed. The alignment and organization of streaks increase with the increase in  $\phi_m$ , while their number reduces. Fewer turbulence streaks in the flow should reduce turbulence. On the other hand, the strength of straightly aligned structures in PLC flow increases with  $\phi_m$ , which may enhance turbulence (Zhou *et al.* 2020). The two competitive mechanisms modulate the turbulent kinetic energy as shown in figure 4. The presence of high-density particle streaks in the LSS region can also be noticed in the figure. The spanwise spacing between the particle streaks aligns well with that between the LSS. Similar to the turbulent streaks, the particle streaks are also



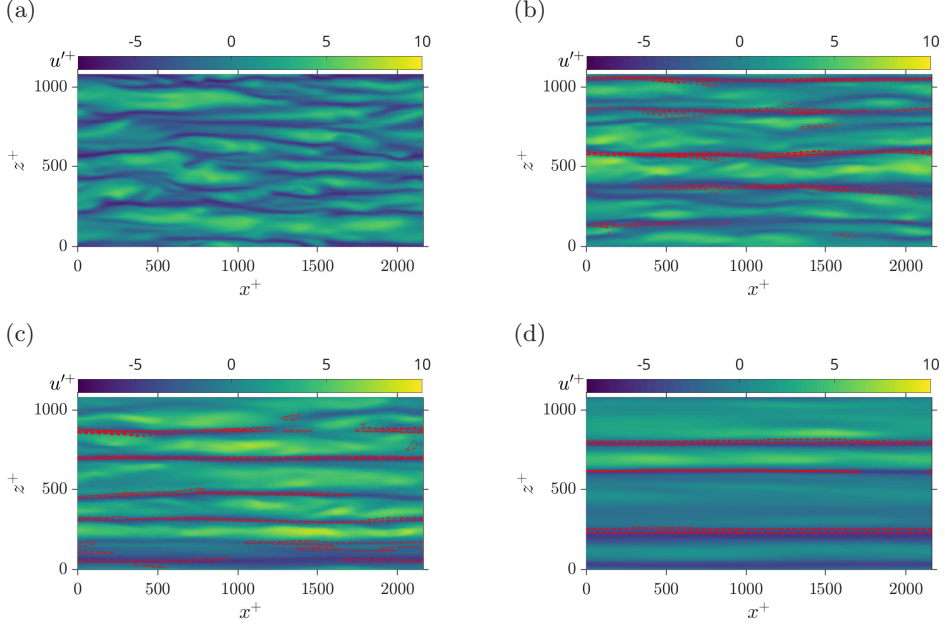


Figure 14: Contours showing the streaks of streamwise velocity fluctuations, overlaid by the red contours of relative particle volume fraction ( $\phi_v > 2.5\bar{\phi}_{vp}$ ), in the spanwise plane at  $y^+ \approx 10$  for  $St^+ = 30$  at (a)  $\phi_m = 0.0$ , (b)  $\phi_m = 0.2$ , (c)  $\phi_m = 0.6$ , and (d)  $\phi_m = 1.0$ . Instantaneous data at the same time instants as in figure 11 is analyzed.

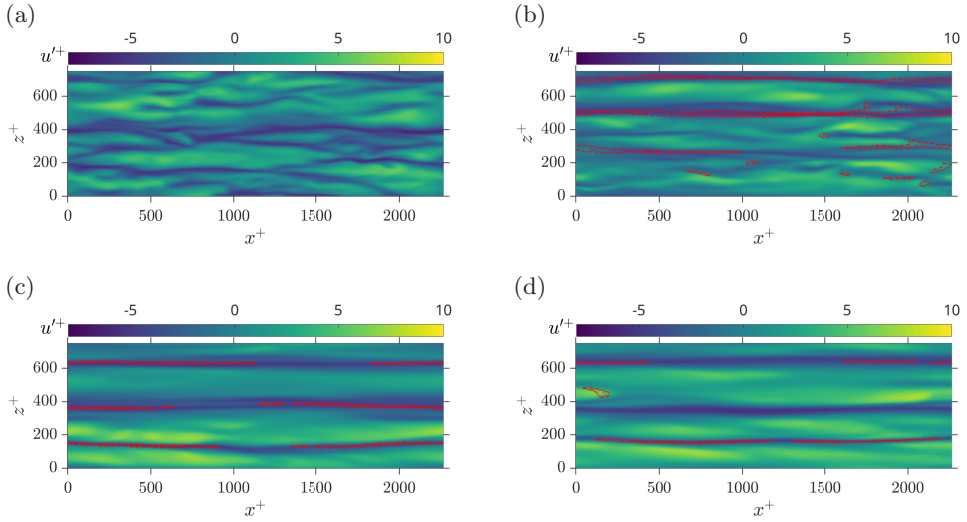


Figure 15: Contours showing the streaks of streamwise velocity fluctuations, overlaid by the red contours of relative particle volume fraction ( $\phi_v > 2.5\bar{\phi}_{vp}$ ), in the spanwise plane at  $y^+ \approx 15$  for  $St^+ = 6$  at (a)  $\phi_m = 0.0$ , (b)  $\phi_m = 0.2$ , (c)  $\phi_m = 0.6$ , and (d)  $\phi_m = 1.0$ . Instantaneous data at the same time instants as in figure 11 is analyzed.

elongated. Thus, it can be concluded that particle streaks are interlinked to low-speed turbulence streaks and contribute to the modulation of flow turbulence.

A similar analysis of PLC flows with  $St^+ = 6$  is presented in figure 15. The effect of particles on the turbulent streaks is similar to those found in the case of PLC flows with  $St^+ = 30$ . Turbulent structures are more aligned at higher  $\phi_m$ , with the particle streaks being present in the region of LSS. Similar to  $St^+ = 30$ , it can be noticed here that for the threshold value of  $\phi_v > 2.5\bar{\phi}_{vp}$ , the presence of particle streaks decreases as  $\phi_m$  increases. At higher  $\phi_m = 0.6$  and  $1.0$ , we observe the absence of particle streaks in some LSS regions. The presence of particle streaks is also lower than that in the PLC flows with  $St^+ = 30$ . However, referring to table 2, it is possible that for a lower threshold value, more particle streaks will be present at higher  $\phi_m$  and lower  $St^+$ . Thus, this observation on the effect of particle  $St^+$  and  $\phi_m$  on particle streaks might change with the selection of the threshold value. Nevertheless, it can be concluded that these highly clustered streaks will appear in LSS in all the cases.

## 5. Concluding Remarks

By extending the quadrature three-order moment method to solve the particle field in a channel flow, we have demonstrated the capability and efficiency of this Eulerian approach in simulating dispersed particle-laden turbulent flows containing a vast number of particles. This method offers a computationally less expensive alternative to the Lagrangian approach, which requires tracking each particle individually. The method is coupled with a compressible flow solver, adapted for incompressible flow with reduced numerical dissipation. Two-way coupling between the fluid and particles has been modelled using Stokes drag. The complete solver is developed in a GPU-accelerated framework.

We have demonstrated the quadrature method's ability to predict the impact of particles on various fluid-particle interactions, such as mean flow and turbulence modulation, drag between fluid and particles, particle migration toward the wall, and preferential clustering, which compares with prior studies using the Lagrangian particle tracking approach. Furthermore, the effects of Stokes number and particle mass loading on these phenomena have been analyzed in detail. The roles of particle migration to the wall and preferential clustering in modulating flow dynamics were also discussed.

Our findings reveal that introducing particles to the fluid increases the mean streamwise velocity, regardless of the Stokes number, though particle mass loading influences this increase. Up to a certain limit, adding more particles enhances the velocity, but beyond that, further particle addition reduces the mean velocity due to increased drag. Using the quadrature method, we show that particles increase overall turbulence in the flow by amplifying streamwise velocity fluctuations while dampening fluctuations in the other two directions. However, at higher mass loadings, low Stokes number cases display a reduction in turbulence. This is due to near-wall preferential clustering of particles in the low turbulence regions, which is more significant for low inertia particles. These clusters of particles modulate the turbulence by interacting with the turbulence streaks.

Particles cluster preferentially along the low turbulence streaks in the near-wall region. Though this preferential clustering is more significant for low inertia particles, it is mostly unaffected by the particle mass loading when the Stokes number is less. At higher Stokes number, preferential clustering increases with the increase in particle mass loading. By interacting with these streaks, particles align the streaks along the streamwise direction. The number of streaks decreases with the addition of more particles, which can reduce turbulence. However, they get more aligned and organized, thus enhancing their strength. The two competitive phenomena affect the overall flow turbulence.

By dampening the wall-normal velocity fluctuations, the addition of particles reduces the Reynolds shear stress in the fluid phase. However, by modelling the total stress balance in the streamwise direction, we show the inclusion of Reynolds shear stress in the particle phase, which increases with the addition of more particles. This stress is due to the drag between the two phases, which is negative near the wall and positive near the channel center. This is due to particles having a higher velocity than the fluid phase in the near-wall region, which arises from the reflective wall boundary condition as opposed to the no-slip wall condition for the fluid. As the particle mass loading increases, the magnitudes of both positive and negative drags increase, and so does the particle Reynolds shear stress. Notably, the Stokes number and particle mass loading affect the location where drag changes sign from positive to negative, with higher mass loadings and lower Stokes numbers shifting this point closer to the channel center. This behavior is explained by particle migration toward the wall due to turbophoresis.

Particle concentrations near the channel center increase with higher mass loadings, resulting in more positive drag between the two phases. As a result, particles and fluid reach the same velocity sooner when the loading is higher, causing the drag to switch at a shorter distance from the center. For the same mass loading, low inertia particles have lower concentrations near the wall and, therefore, produce less negative drag compared to high inertia particles. However, because low inertia particles have higher concentrations near the channel center, the positive drag is greater in flows loaded with low inertia particles. This further allows for earlier switching of the drag profile when the Stokes number is less.

Thus, our results using the Eulerian quadrature moment-based method reveal the physics between the particle accumulation toward the wall and the drag between the two phases, which influence the particle Reynolds shear stress and, consequently, the viscous stress in the fluid. Our method also predicts the interplay between the particle preferential clustering and turbulence streaks near the wall, which modifies flow turbulence. The study presents the Eulerian particle-fluid solvers that can be extended for future research on a wide range of multiphase flow phenomena of practical interest.

## Acknowledgement

This research was supported by the ISRAEL SCIENCE FOUNDATION (grant No. 1762/20).

## Appendix A. CFD Matrix

The appendix details the matrix of all fluid and particle variables used in the CFD simulation. Each row of the matrix corresponds to a particular equation in the transport model represented by Eq. 2.3.

$$C_f = \begin{bmatrix} \rho \\ \rho u \\ \rho v \\ \rho w \\ \rho e \end{bmatrix} \quad \vec{F}_f = \begin{bmatrix} \rho \vec{V} \\ \rho u \vec{V} + P \hat{n}_x \\ \rho v \vec{V} + P \hat{n}_y \\ \rho w \vec{V} + P \hat{n}_z \\ (\rho e + P) \vec{V} \end{bmatrix} \quad \vec{S}_v = \begin{bmatrix} 0 \\ \tau_{xx} \hat{n}_x + \tau_{xy} \hat{n}_y + \tau_{xz} \hat{n}_z \\ \tau_{xy} \hat{n}_x + \tau_{yy} \hat{n}_y + \tau_{yz} \hat{n}_z \\ \tau_{xz} \hat{n}_x + \tau_{yz} \hat{n}_y + \tau_{zz} \hat{n}_z \\ q_x \hat{n}_x + q_y \hat{n}_y + q_z \hat{n}_z \end{bmatrix} \quad S_{c_f} = \begin{bmatrix} 0 \\ -F_{Dx} \\ -F_{Dy} \\ -F_{Dz} \\ -E_D \end{bmatrix}$$

$$C_p = \begin{bmatrix} M^0 \\ M_x^1 \\ M_y^1 \\ M_z^1 \\ M_{xx}^2 \\ M_{yy}^2 \\ M_{zz}^2 \\ Q \end{bmatrix} \quad \vec{F}_p = \begin{bmatrix} M_x^1 \hat{x} + M_y^1 \hat{y} + M_z^1 \hat{z} \\ M_{xx}^2 \hat{x} + M_{xy}^2 \hat{y} + M_{xz}^2 \hat{z} \\ M_{yx}^2 \hat{x} + M_{yy}^2 \hat{y} + M_{yz}^2 \hat{z} \\ M_{zx}^2 \hat{x} + M_{zy}^2 \hat{y} + M_{zz}^2 \hat{z} \\ M_{xxx}^3 \hat{x} + M_{xxy}^3 \hat{y} + M_{xxz}^3 \hat{z} \\ M_{yyx}^3 \hat{x} + M_{yyy}^3 \hat{y} + M_{yyz}^3 \hat{z} \\ M_{zzx}^3 \hat{x} + M_{zzy}^3 \hat{y} + M_{zzz}^3 \hat{z} \\ R_x \hat{x} + R_y \hat{y} + R_z \hat{z} \end{bmatrix}$$

$$S_{c_p} = \begin{bmatrix} 0 \\ \frac{\rho_{p1}}{m_p} F_{Dx1} + \frac{\rho_{p2}}{m_p} F_{Dx2} \\ \frac{\rho_{p1}}{m_p} F_{Dy1} + \frac{\rho_{p2}}{m_p} F_{Dy2} \\ \frac{\rho_{p1}}{m_p} F_{Dz1} + \frac{\rho_{p2}}{m_p} F_{Dz2} \\ 2 \frac{\rho_{p1}}{m_p} u_{p1} F_{Dx1} + 2 \frac{\rho_{p2}}{m_p} u_{p2} F_{Dx2} \\ 2 \frac{\rho_{p1}}{m_p} v_{p1} F_{Dy1} + 2 \frac{\rho_{p2}}{m_p} v_{p2} F_{Dy2} \\ 2 \frac{\rho_{p1}}{m_p} w_{p1} F_{Dz1} + 2 \frac{\rho_{p2}}{m_p} w_{p2} F_{Dz2} \\ \sum_{x,y,z} 3(U_{p1}^2 F_{D1}) \frac{\rho_{p1}}{m_p} + 3 \frac{\rho_{p2}}{m_p} \sum_{x,y,z} (U_{p2}^2 F_{D2}) \end{bmatrix}$$

## REFERENCES

- ANGILELLA, JEAN-RÉGIS 2010 Dust trapping in vortex pairs. *Physica D: Nonlinear Phenomena* **239**, 1789–1797.
- AVNI, ORR & DAGAN, YUVAL 2022a Dispersion of free-falling saliva droplets by two-dimensional vortical flows. *Theoretical and Computational Fluid Dynamics* **36**, 993–1011.
- AVNI, ORR & DAGAN, YUVAL 2022b Dynamics of evaporating respiratory droplets in the vicinity of vortex dipoles. *International Journal of Multiphase Flow* **148**, 103901.
- AVNI, ORR & DAGAN, YUVAL 2023a Droplet dynamics in burgers vortices. I. mass transport. *Physical Review Fluids* **8** (8), 083604.
- AVNI, ORR & DAGAN, YUVAL 2023b Droplet dynamics in burgers vortices. II. heat transfer. *Physical Review Fluids* **8** (8), 083605.
- BAKER, MICHAEL, KONG, BO, CAPECELATRO, JESSE, DESJARDINS, OLIVIER & FOX, RODNEY 2020 Verification of eulerian-eulerian and eulerian-lagrangian simulations for particle-laden vertical channel flow. *Authorea Preprints* .
- BALACHANDAR, S. & EATON, JOHN K. 2010a Turbulent dispersed multiphase flow. *Annual Review of Fluid Mechanics* **42**, 111–133.
- BALACHANDAR, S & EATON, JOHN K 2010b Turbulent dispersed multiphase flow. *Annual review of fluid mechanics* **42**, 111–133.
- BERK, TIM & COLETTI, FILIPPO 2023 Dynamics and scaling of particle streaks in high-reynolds-number turbulent boundary layers. *Journal of Fluid Mechanics* **975**, A47.
- BJÖRCK, ÅKE 1996 *Numerical methods for least squares problems*. SIAM.
- BOUCHUT, F 1994 On zero pressure gas dynamics. advances in kinetic theory and computing, series on advances in mathematics for applied sciences 22.
- CAPORALONI, M, TAMPIERI, F, TROMBETTI, F & VITTORI, O 1975 Transfer of particles in nonisotropic air turbulence. *Journal of the atmospheric sciences* **32** (3), 565–568.
- CHEN, SHU-SHENG, CAI, FANG-JIE, XUE, HAI-CHAO, WANG, NING & YAN, CHAO 2020 An improved ausm-family scheme with robustness and accuracy for all mach number flows. *Applied Mathematical Modelling* **77**, 1065–1081.
- COOK, SHANE 2012 *CUDA programming: a developer's guide to parallel computing with GPUs*. Newnes.
- DAGAN, YUVAL 2021 Settling of particles in the vicinity of vortex flows. *Atomization and Sprays* **31** (11).
- DAGAN, YUVAL, ARAD, ERAN & TAMBOUR, YORAM 2015 On the dynamics of spray flames in turbulent flows. *Proceedings of the Combustion Institute* **35** (2), 1657–1665.
- DAGAN, Y, ARAD, E & TAMBOUR, Y 2016 The evolution of local instability regions in turbulent non-premixed flames. *Journal of Fluid Mechanics* **803**, 18–50.
- DAGAN, Y., GREENBERG, J.B. & KATOSHEVSKI, D. 2017a Similarity solutions for the evolution of polydisperse droplets in vortex flows. *International Journal of Multiphase Flow* **97**, 1–9.
- DAGAN, Y., KATOSHEVSKI, D. & GREENBERG, J. B. 2017b Particle and droplet clustering in oscillatory vortical flows. *Atomization and Sprays* **27**, 629–643.
- DAGAN, Y., KATOSHEVSKI, D. & GREENBERG, J. B. 2018 Similarity solutions for the evolution of unsteady spray diffusion flames in vortex flows. *Combustion Science and Technology* **190**, 1110–1125.
- DAVE, HIMANSHU & KASBAOUI, M HOUSSEM 2023 Mechanisms of drag reduction by semidilute inertial particles in turbulent channel flow. *Physical Review Fluids* **8** (8), 084305.
- DESHPANDE, SURESH M 1986 A second-order accurate kinetic-theory-based method for inviscid compressible flows. *Tech. Rep.*.
- DESJARDINS, O, FOX, RODNEY & VILLEDIEU, P 2006 A quadrature-based moment closure for the williams spray equation .
- DESJARDINS, OLIVIER, FOX, RODNEY O & VILLEDIEU, PHILIPPE 2008 A quadrature-based moment method for dilute fluid-particle flows. *Journal of Computational Physics* **227** (4), 2514–2539.
- DRUZHININ, OA 1994 Concentration waves and flow modification in a particle-laden circular vortex. *Physics of Fluids* **6** (10), 3276–3284.
- DRUZHININ, OA 1995 On the two-way interaction in two-dimensional particle-laden flows: the accumulation of particles and flow modification. *Journal of Fluid Mechanics* **297**, 49–76.

- EATON, JOHN K & FESSLER, JR1134 1994 Preferential concentration of particles by turbulence. *International Journal of Multiphase Flow* **20**, 169–209.
- ESTIVALEZES, JL & VILLEDIEU, P 1996 High-order positivity-preserving kinetic schemes for the compressible euler equations. *SIAM journal on numerical analysis* **33** (5), 2050–2067.
- FONG, KEE ONN, AMILI, OMID & COLETTI, FILIPPO 2019 Velocity and spatial distribution of inertial particles in a turbulent channel flow. *Journal of Fluid Mechanics* **872**, 367–406.
- FOX, RODNEY O 2012 Large-eddy-simulation tools for multiphase flows. *Annual Review of Fluid Mechanics* **44** (1), 47–76.
- FOX, RODNEY O, LAURENT, FRÉDÉRIQUE & MASSOT, MARC 2008 Numerical simulation of spray coalescence in an eulerian framework: direct quadrature method of moments and multi-fluid method. *Journal of Computational Physics* **227** (6), 3058–3088.
- HEYLMUN, JEFFREY C, FOX, RODNEY O & PASSALACQUA, ALBERTO 2021 A quadrature-based moment method for the evolution of the joint size-velocity number density function of a particle population. *Computer Physics Communications* **267**, 108072.
- IJZERMANS, RUTGER H.A. & HAGMEIJER, ROB 2006 Accumulation of heavy particles in n-vortex flow on a disk. *Physics of Fluids* **18**, 063601.
- JOHNSON, PERRY L, BASSENNE, MAXIME & MOIN, PARVIZ 2020 Turbophoresis of small inertial particles: theoretical considerations and application to wall-modelled large-eddy simulations. *Journal of Fluid Mechanics* **883**, A27.
- KASBAOUI, M HOUSSEM 2019 Turbulence modulation by settling inertial aerosols in eulerian-eulerian and eulerian-lagrangian simulations of homogeneously sheared turbulence. *Physical Review Fluids* **4** (12), 124308.
- KASBAOUI, M HOUSSEM, KOCH, DONALD L & DESJARDINS, OLIVIER 2019 Clustering in euler-euler and euler-lagrange simulations of unbounded homogeneous particle-laden shear. *journal of fluid mechanics* **859**, 174–203.
- KITAMURA, KEIICHI & HASHIMOTO, ATSUSHI 2016 Reduced dissipation ausm-family fluxes: Hrslau2 and hr-ausm+-up for high resolution unsteady flow simulations. *Computers & Fluids* **126**, 41–57.
- KITAMURA, KEIICHI & SHIMA, EIJI 2010 Improvements of simple low-dissipation ausm against shock instabilities in consideration of interfacial speed of sound. In *Proceedings of ECCOMAS CFD*, , vol. 1283.
- KITAMURA, KEIICHI & SHIMA, EIJI 2013 Towards shock-stable and accurate hypersonic heating computations: A new pressure flux for ausm-family schemes. *Journal of Computational Physics* **245**, 62–83.
- KOKKINAKIS, IOANNIS WILLIAM 2009 Investigation of high-resolution methods in large-eddy simulation of subsonic and supersonic wall turbulent flows .
- KONG, BO, FOX, RODNEY O, FENG, HENG, CAPECELATRO, JESSE, PATEL, RAVI, DESJARDINS, OLIVIER & FOX, RODNEY O 2017 Euler–euler anisotropic gaussian mesoscale simulation of homogeneous cluster-induced gas–particle turbulence. *AIChE Journal* **63** (7), 2630–2643.
- KUERTEN, JGM VD, VAN DER GELD, CWM & GEURTS, BERNARDUS J 2011 Turbulence modification and heat transfer enhancement by inertial particles in turbulent channel flow. *Physics of fluids* **23** (12).
- KULICK, JONATHAN D, FESSLER, JOHN R & EATON, JOHN K 1994 Particle response and turbulence modification in fully developed channel flow. *Journal of Fluid Mechanics* **277**, 109–134.
- KUSSIN, J & SOMMERFELD, M 2002 Experimental studies on particle behaviour and turbulence modification in horizontal channel flow with different wall roughness. *Experiments in Fluids* **33** (1), 143–159.
- LEE, JUNGHOON & LEE, CHANGHOON 2015 Modification of particle-laden near-wall turbulence: Effect of stokes number. *Physics of Fluids* **27** (2).
- LIU, MENG-SING 1996 A sequel to ausm: Ausm+. *Journal of computational Physics* **129** (2), 364–382.
- LIU, MENG-SING 2006 A sequel to ausm, part ii: Ausm+-up for all speeds. *Journal of computational physics* **214** (1), 137–170.
- LIU, MENG-SING & STEFFEN JR, CHRISTOPHER J 1993 A new flux splitting scheme. *Journal of Computational physics* **107** (1), 23–39.
- MAMASHITA, TOMOHIRO, KITAMURA, KEIICHI & MINOSHIMA, TAKASHI 2021 Slau2-mhd for low



- mach magnetohydrodynamics (mhd) simulations. In *AIAA AVIATION 2021 FORUM*, p. 2730.
- MARCHIOLI, CRISTIAN & SOLDATI, ALFREDO 2002 Mechanisms for particle transfer and segregation in a turbulent boundary layer. *Journal of fluid Mechanics* **468**, 283–315.
- MARCHISIO, DANIELE L. & FOX, RODNEY O. 2013 *Mesoscale description of polydisperse systems*, p. 30–46. Cambridge University Press.
- MARCU, B. & MEIBURG, E. 1996*a* The effect of streamwise braid vortices on the particle dispersion in a plane mixing layer. i. equilibrium points and their stability. *Physics of Fluids* **8**, 715–733.
- MARCU, B. & MEIBURG, E. 1996*b* Three-dimensional features of particle dispersion in a nominally plane mixing layer. *Physics of Fluids* **8**, 2266–2268.
- MARCU, B., MEIBURG, E. & NEWTON, P. K. 1995 Dynamics of heavy particles in a burgers vortex. *Physics of Fluids* **7**, 400–410.
- MARCU, B, MEIBURG, E & RAJU, N 1996 The effect of streamwise braid vortices on the particle dispersion in a plane mixing layer. ii. nonlinear particle dynamics articles you may be interested in. *Physics of Fluids* **8**, 734.
- MATSUYAMA, SHINGO 2014 Performance of all-speed ausm-family schemes for dns of low mach number turbulent channel flow. *Computers & Fluids* **91**, 130–143.
- MCLAUGHLIN, JOHN B 1989 Aerosol particle deposition in numerically simulated channel flow. *Physics of Fluids A: Fluid Dynamics* **1** (7), 1211–1224.
- MEHTA, RC & JAYACHANDRAN, T 1998 A fast algorithm to solve viscous two-phase flow in an axisymmetric rocket nozzle. *International journal for numerical methods in fluids* **26** (5), 501–517.
- MOSER, ROBERT D, KIM, JOHN & MANSOUR, NAGI N 1999 Direct numerical simulation of turbulent channel flow up to  $Re_\tau = 590$ . *Physics of fluids* **11** (4), 943–945.
- NOWBAHAR, ARASH, SARDINA, GAETANO, PICANO, FRANCESCO & BRANDT, LUCA 2013 Turbophoresis attenuation in a turbulent channel flow with polymer additives. *Journal of Fluid Mechanics* **732**, 706–719.
- PENG, CHENG, WANG, LIAN-PING & CHEN, SONGYING 2024 Preferential accumulation of finite-size particles in near-wall streaks. *Journal of Fluid Mechanics* **980**, A38.
- PERTHAME, BENOIT 1992 Second-order boltzmann schemes for compressible euler equations in one and two space dimensions. *SIAM Journal on Numerical Analysis* **29** (1), 1–19.
- POPE, STEPHEN B. 2000 *Turbulent Flows*. Cambridge University Press.
- PULLIN, DI 1980 Direct simulation methods for compressible inviscid ideal-gas flow. *Journal of Computational Physics* **34** (2), 231–244.
- RAVICHANDRAN, S. & GOVINDARAJAN, RAMA 2022 Waltz of tiny droplets and the flow they live in. *Physical Review Fluids* **7**, 110512.
- REEKS, MW 1983 The transport of discrete particles in inhomogeneous turbulence. *Journal of aerosol science* **14** (6), 729–739.
- SAFFMAN, PHILIP GEOFFREY 1965 The lift on a small sphere in a slow shear flow. *Journal of fluid mechanics* **22** (2), 385–400.
- SALMAN, HAYDER & SOTERIOU, MARIOS 2004 Lagrangian simulation of evaporating droplet sprays. *Physics of Fluids* **16** (12), 4601–4622.
- SANDERS, JASON 2010 *CUDA by Example: An Introduction to General-Purpose GPU Programming*. Addison Wesley.
- SARDINA, GAETANO, SCHLATTER, PHILIPP, BRANDT, LUCA, PICANO, FRANCESCO & CASCIOLA, CARLO MASSIMO 2012 Wall accumulation and spatial localization in particle-laden wall flows. *Journal of Fluid Mechanics* **699**, 50–78.
- SCHNEIDERBAUER, SIMON & SAEEDIPOUR, MAHDI 2019 Numerical simulation of turbulent gas–solid flow using an approximate deconvolution model. *International Journal of Multiphase Flow* **114**, 287–302.
- SHIMA, ELJI 2013 On the improvement of the all-speed flux scheme for very low mach number flows. In *21st AIAA Computational Fluid Dynamics Conference*, p. 2696.
- SHIMA, ELJI & KITAMURA, KEIICHI 2011 Parameter-free simple low-dissipation ausm-family scheme for all speeds. *AIAA journal* **49** (8), 1693–1709.
- SIKOVSKY, DMITRII PH 2014 Singularity of inertial particle concentration in the viscous sublayer of wall-bounded turbulent flows. *Flow, turbulence and combustion* **92**, 41–64.



- SQUIRES, KD & EATON, JK 1994 Effect of selective modification of turbulence on two-equation models for particle-laden turbulent flows .
- SQUIRES, KYLE D & EATON, JOHN K 1990 Particle response and turbulence modification in isotropic turbulence. *Physics of Fluids A: Fluid Dynamics* **2** (7), 1191–1203.
- SQUIRES, KYLE D & EATON, JOHN K 1991 Preferential concentration of particles by turbulence. *Physics of Fluids A: Fluid Dynamics* **3** (5), 1169–1178.
- THORNER, BEN, DRIKAKIS, DIMITRIS, WILLIAMS, ROBIN JR & YOUNGS, DAVID 2008*a* On entropy generation and dissipation of kinetic energy in high-resolution shock-capturing schemes. *Journal of Computational Physics* **227** (10), 4853–4872.
- THORNER, BEN, MOSEDALE, ANDREW, DRIKAKIS, DIMITRIS, YOUNGS, DAVID & WILLIAMS, ROBIN JR 2008*b* An improved reconstruction method for compressible flows with low mach number features. *Journal of computational Physics* **227** (10), 4873–4894.
- TORO, ELEUTERIO F 2019 The hllc riemann solver. *Shock waves* **29** (8), 1065–1082.
- TORO, ELEUTERIO F, SPRUCE, MICHAEL & SPEARES, WILLIAM 1994 Restoration of the contact surface in the hll-riemann solver. *Shock waves* **4**, 25–34.
- VENKATAKRISHNAN, VENKAT 1993 On the accuracy of limiters and convergence to steady state solutions. In *31st Aerospace Sciences Meeting*, p. 880.
- VENKATAKRISHNAN, VENKAT 1995 Convergence to steady state solutions of the euler equations on unstructured grids with limiters. *Journal of computational physics* **118** (1), 120–130.
- VIÉ, AYMERIC, DOISNEAU, FRANÇOIS & MASSOT, MARC 2015 On the anisotropic gaussian velocity closure for inertial-particle laden flows. *Communications in Computational Physics* **17** (1), 1–46.
- VREMAN, BERT, GEURTS, BERNARD J, DEEN, NG, KUIPERS, JAM & KUERTEN, JOHANNES GM 2009 Two-and four-way coupled euler–lagrangian large-eddy simulation of turbulent particle-laden channel flow. *Flow, turbulence and combustion* **82** (1), 47–71.
- WILLIAMS, FORMAN A 1958 Spray combustion and atomization. *The physics of fluids* **1** (6), 541–545.
- YERASI, SUMITHRA REDDY, GOVINDARAJAN, RAMA & VINCENZI, DARIO 2022 Spirographic motion in a vortex. *Physical Review Fluids* **7**, 074402.
- ZHANG, DZ & PROSPERETTI, A 1994 Averaged equations for inviscid disperse two-phase flow. *Journal of Fluid Mechanics* **267**, 185–219.
- ZHANG, DZ & PROSPERETTI, A 1997 Momentum and energy equations for disperse two-phase flows and their closure for dilute suspensions. *International journal of multiphase flow* **23** (3), 425–453.
- ZHAO, LH, ANDERSSON, HELGE I & GILLISSEN, JJJ 2010 Turbulence modulation and drag reduction by spherical particles. *Physics of Fluids* **22** (8), 081702.
- ZHAO, LIHAO, ANDERSSON, HELGE I & GILLISSEN, JURRIAAN JJ 2013 Interphasial energy transfer and particle dissipation in particle-laden wall turbulence. *Journal of Fluid Mechanics* **715**, 32–59.
- ZHOU, TIAN, ZHAO, LIHAO, HUANG, WEIXI & XU, CHUNXIAO 2020 Non-monotonic effect of mass loading on turbulence modulations in particle-laden channel flow. *Physics of Fluids* **32** (4), 043304.